

# Outstanding thermoelectric performance predicted for out-of-plane p-doped GeSe

Anderson S. Chaves,<sup>1,2</sup> Daniel T. Larson,<sup>3</sup> Efthimios Kaxiras,<sup>3,2</sup> and Alex Antonelli<sup>4</sup>

<sup>1</sup>*Gleb Wataghin Institute of Physics, University of Campinas, PO Box 13083-859, Campinas, SP, Brazil*

<sup>2</sup>*John A. Paulson School of Engineering and Applied Sciences,  
Harvard University, Cambridge, Massachusetts, 02138, USA*

<sup>3</sup>*Department of Physics, Harvard University, Cambridge, Massachusetts, 02138, USA*

<sup>4</sup>*Gleb Wataghin Institute of Physics and Center for Computing in Engineering & Sciences,  
University of Campinas, PO Box 13083-859, Campinas, SP, Brazil*

(Dated: February 15, 2022)

The record-breaking thermoelectric performance of tin selenide (SnSe) has motivated the investigation of analogue compounds with the same structure. A promising candidate that emerged recently is germanium selenide (GeSe). Here, using extensive first-principles calculations of the hole-phonon and hole-impurity scattering, we investigate the thermoelectric transport properties of the orthorhombic phase of p-doped GeSe. We predict outstanding thermoelectric performance for GeSe over a broad range of temperatures due to its high Seebeck coefficients, extremely low Lorenz numbers, ultralow total thermal conductivity, and relatively large band gap. In particular, the out-of-plane direction in GeSe presents equivalent or even higher performance than SnSe for temperatures above 500 K. By extending the analysis to 900 K, we obtained an ultrahigh value for the thermoelectric figure of merit ( $zT = 3.2$ ) at the optimal hole density of  $4 \times 10^{19} \text{ cm}^{-3}$ . Our work provides strong motivation for continued experimental work focusing on improving the GeSe doping efficiency in order to achieve this optimal hole density.

## I. Introduction

High-efficiency thermoelectric (TE) materials have been systematically and comprehensively investigated during the past several decades, mainly due to their capability of functioning as all-solid-state modules for distributed spot-size refrigeration[1, 2] or electric power generation from waste heat.[3, 4] The key quantity to evaluate the efficiency of TE energy conversion is the dimensionless figure of merit,  $zT = \sigma S^2 T / \kappa_{\text{tot}}$ , where  $\sigma$ ,  $S$ ,  $T$  stand for the electrical conductivity, the Seebeck coefficient, and the absolute temperature and  $\kappa_{\text{tot}} = \kappa_{\text{latt}} + \kappa_{\text{h}}$  is the total thermal conductivity, comprised of lattice and electronic carrier contributions, respectively. Numerous TE materials have been discovered, and a few of them even have  $zT$  values between 2 and 3[5–15]. However, even those high- $zT$  materials do not have sufficient efficiency to be largely employed by industry[3, 4, 16]. Indeed, it has been argued that materials with  $zT > 3$  would represent a highly attractive prospect for applications, allowing TE refrigerators to compete with traditional compressor-based refrigerators[1, 17]. Such ultrahigh  $zT$  values have not been measured in bulk materials until very recently.[18] Thus, TE materials have so far only found niche applications where reliability is of higher priority than efficiency.

The figure of merit,  $zT$ , can be enhanced either by increasing the power factor ( $PF = \sigma S^2$ ) or reducing the thermal conductivity,  $\kappa_{\text{tot}}$ . Ultimately, the main goal is to find TE materials that satisfy both of these conditions simultaneously, which is a challenge since the properties involved are interdependent. The maximization of  $PF$  relies on band-structure engineering[19–21] such as increasing band degeneracy through convergence of bands [22, 23] or taking advantage of band structure

anisotropy[24] and non-parabolicity [25]. On the other hand, the main strategies to minimize  $\kappa_{\text{tot}}$  include identifying materials with intrinsically low  $\kappa_{\text{latt}}$ [26], minimizing the electronic carrier contribution,  $\kappa_{\text{h}}$ , through the minimization of the Lorenz function[27, 28], or by alloying or nanostructuring procedures[22, 29–32]. Despite the challenges, impressive achievements have been obtained on the basis of such strategies [4, 12, 33–38].

The record-breaking TE performance of SnSe[13–15] has motivated the investigation of analogue IV–VI compounds with the same puckered layer structure, in order to ascertain whether such systems also possess inherently low  $\kappa_{\text{latt}}$  and high  $zT$ . A promising candidate is germanium selenide (GeSe), which, like SnSe, crystallizes in the orthorhombic GeS-type structure shown in Fig. 1, with a space group of  $D_{2h}^{16} (Pnma)$ [39, 40].

Additional advantages that make GeSe very attractive for large applications in thermoelectrics and photovoltaics include chemical stability, earth-abundance, environmental compatibility and low toxicity (no lead).[41–45] Recently, theoretical work by Ding *et al.*[46] put forward the possibility of achieving large  $S$  and  $PF$  values by proper p- or n-type doping of GeSe. Due to low thermal conductivity and multiband effects, Hao *et al.*[47] predicted an ultrahigh peak  $zT$  value of 2.5 along the in-plane (b-axis) direction of the orthorhombic phase of GeSe with a hole density of  $6.5 \times 10^{19} \text{ cm}^{-3}$  at 800 K. If this could be realized, it would outperform p-doped SnSe. Though highly suggestive, that prediction used the same values for relaxation times and carrier densities as those reported for p-doped SnSe. Despite the great potential of the orthorhombic phase of GeSe for TE applications, there are still relatively few published experimental results[48].

In the present work we examine the thermoelectric per-

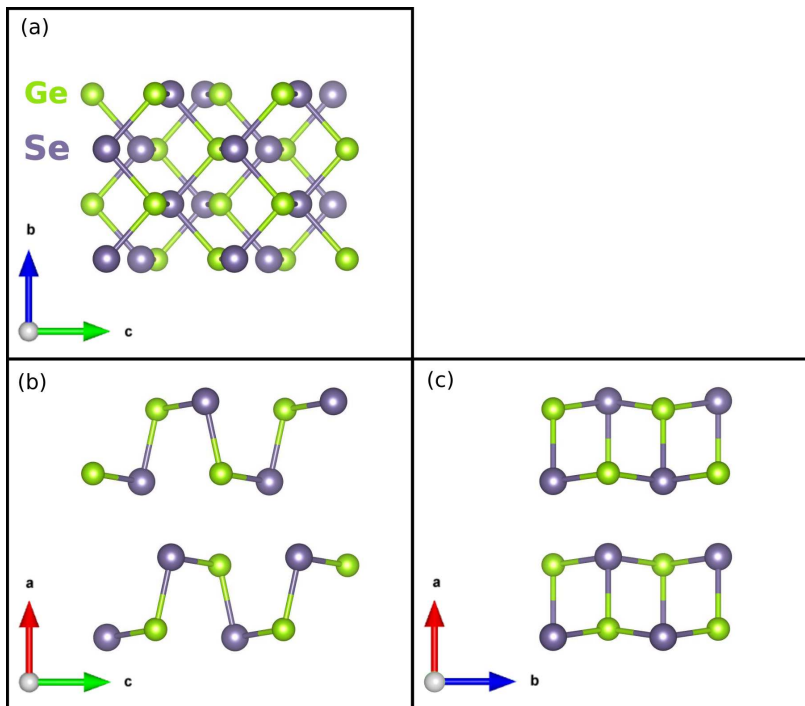


Figure 1: Crystal structure of  $Pnma$  GeSe with views along each crystallographic direction: (a) perpendicular to the layer plane, (b,c) along the layer planes. Green and gray spheres represent Ge and Se, respectively.

formance of p-doped GeSe and SnSe within the Boltzmann Transport equation (BTE) formalism, by explicitly calculating relaxation times due to hole-phonon (h-p) and hole-impurity couplings using a comprehensive first-principles approach. In particular, the hole-phonon coupling was calculated by using the dual interpolation scheme[49] of the density functional theory (DFT) band structure[50, 51]. The phonon dispersion and h-p matrix elements were determined by density functional perturbation theory (DFPT)[52]. The carrier density for the different axes was derived from the record-breaking transport data measured in p-doped SnSe[14]. The calculated temperature and energy dependent relaxation times allow for a deeper understanding of the microscopic processes underlying the temperature-dependent transport phenomena in p-doped GeSe and SnSe.

Our results predict a very high figure of merit for both out-of-plane (a-axis) and in-plane (c-axis) GeSe in a broad range of temperatures. This can be attributed to several factors that synergistically influence the performance: high Seebeck coefficients, extremely low Lorenz numbers, low hole thermal conductivities, very low lattice thermal conductivity, and a relatively large band gap. In fact, for temperatures above 500 K, out-of-plane GeSe is predicted to potentially have a higher  $zT$  than the record-breaking SnSe. By extending the analysis to 900 K, we obtain the outstanding  $zT$  values of 3.2 and 2.8 for the out-of-plane and in-plane directions with optimal carrier densities of  $4 \times 10^{19} \text{ cm}^{-3}$  and  $5 \times 10^{19} \text{ cm}^{-3}$ , respectively. We find that the total relaxation time for the out-of-plane

direction in GeSe is much higher than the corresponding relaxation time in SnSe, demonstrating the importance of directly calculating the relaxation times for GeSe.

## II. Theoretical Approach

The hole-phonon (h-p) coupling and the scattering of holes by ionized impurities are the microscopic processes that determine the temperature-dependent p-type transport phenomena in TE materials, such as GeSe and SnSe. We calculate these TE transport properties from first-principles using the many-body perturbation theory of the h-p interaction following the Fan-Migdal approach and the Boltzmann transport formalism. The comprehensive theoretical framework for the calculation of the band ( $n$ ) and momentum ( $\mathbf{k}$ ) resolved relaxation time (RT),  $\tau_{n,\mathbf{k}}$ , is described in detail in our previous work [28] and summarized in the Supplemental Material (SM)[53] for easy reference. In brief, we calculate three contributions to the total relaxation time. The nonpolar RT ( $\tau_{\text{npol}}$ ) comes from the short-range portion of the hole coupling to acoustic and optical phonons, which can be calculated using dual interpolation. The long-range portion of the hole coupling with optical phonons gives rise to the polar RT ( $\tau_{\text{pol}}$ ), which we determine using the analytic Vogl formula [54–56] with the addition of Ehrenreich screening [57]. Finally, extrinsic scattering by ionized impurities ( $\tau_{\text{imp}}$ ) is calculated using the theory developed by Brooks and Herring (B-H) [58, 59], which

has been extended to go beyond the parabolic band approximation.[60]

Assuming these scattering mechanisms can be treated independently, the total RT is determined by Mathiessen's rule, where the dependence of scattering times on independent variables, including temperature ( $T$ ) and chemical potential ( $\mu$ ), is shown explicitly:

$$\frac{1}{\tau_{\text{tot}}(n, \mathbf{k}, \mu, T)} = \frac{1}{\tau_{\text{npol}}(n, \mathbf{k}, T)} + \frac{1}{\tau_{\text{pol}}(n, \mathbf{k}, \mu, T)} + \frac{1}{\tau_{\text{imp}}(n, \mathbf{k}, \mu, T)}. \quad (1)$$

From  $\tau_{\text{tot}}$  we calculate the TE transport coefficients using the semiclassical BTE with the (non-constant) relaxation time approximation (RTA).[60, 61] The key quantity is the momentum- and band-resolved transport distribution kernel,

$$\Sigma_{\alpha, \beta}(n, \mathbf{k}, \mu, T) = e^2 \tau_{n, \mathbf{k}}(\mu, T) v_{\alpha}(n, \mathbf{k}) v_{\beta}(n, \mathbf{k}), \quad (2)$$

where  $\tau_{n, \mathbf{k}}(\mu, T) \equiv \tau_{\text{tot}}$  is the total relaxation time and  $v(n, \mathbf{k})$  is the average group velocity. The energy projected transport function can then be defined as

$$\Sigma_{\alpha, \beta}(\epsilon, \mu, T) = \frac{1}{N_{\mathbf{k}}} \sum_{\mathbf{k}} \Sigma_{\alpha, \beta}(n, \mathbf{k}, \mu, T) \frac{\delta(\epsilon - \epsilon_{n, \mathbf{k}})}{d\epsilon}, \quad (3)$$

and is used to calculate the transport tensors in terms of the different energy moments

$$I_{\alpha, \beta}^{(n)}(T, \mu) = \frac{1}{\Omega} \int \Sigma_{\alpha, \beta}(\epsilon, \mu, T) (\epsilon - \mu)^n \left( -\frac{\partial f_{\mu}(\epsilon, T)}{\partial \epsilon} \right) d\epsilon. \quad (4)$$

With the experimental conditions of zero temperature gradient ( $\nabla T = 0$ ) and zero electric current, the transport tensors yield the electrical conductivity,

$$\sigma \equiv \sigma_{\alpha, \beta}(T, \mu) = I_{\alpha, \beta}^{(0)}(T, \mu), \quad (5)$$

the Seebeck coefficient,

$$S \equiv S_{i, j}(T, \mu) = (eT)^{-1} I_{\alpha, i}^{(1)}(T, \mu) / I_{\alpha, j}^{(0)}(T, \mu), \quad (6)$$

and the charge carrier contribution to the thermal conductivity,

$$\kappa_{\text{h}} \equiv \kappa_{i, j}^{\text{h}}(T, \mu) = (e^2 T)^{-1} \left( I_{i, j}^{(2)}(T, \mu) - I_{i, \alpha}^{(1)}(T, \mu) \cdot I_{\beta, \alpha}^{(0)}(T, \mu)^{-1} \cdot I_{\beta, j}^{(1)}(T, \mu) \right). \quad (7)$$

### III. Computational details

Below are the details for calculations involving GeSe; the details for SnSe can be found in Ref. 28. The relaxed geometry and electronic structure of GeSe was calculated

using DFT, while the phonon dispersions and h-p matrix elements were calculated using DFPT, both implemented in the Quantum Espresso package[62]. We employed fully-relativistic optimized norm-conserving Vanderbilt pseudopotentials[63, 64] within the generalized gradient approximation (GGA) for the exchange-correlation functional according to the formulation of Perdew-Burke-Ernzerhof (PBE)[65]. Monkhorst-Pack grids of  $6 \times 18 \times 14$  for  $\mathbf{k}$ -point sampling and a kinetic energy cutoff of 80 Ry were employed to ensure the convergence of the total energy in DFT calculations. The energy convergence threshold for the total energy difference between two successive self-consistency steps was  $10^{-11}$  Ry under the Davidson-type diagonalization method. Because DFT-GGA calculations underestimate the GeSe band gap, a scissor operator was used to rigidly shift the conduction bands upwards in order to attain the experimental band gap of 1.1 eV [66, 67].

At room temperature both GeSe and SnSe crystallize in a layered orthorhombic structure with the  $Pnma$  space group and 8 atoms in the unit cell, shown in Fig. 1. The melting point of GeSe occurs at  $948 \pm 2$  K,[68–70] but according to Wiedemeier *et al.*[71], at 924K a structural transition takes place from the orthorhombic phase to the ideal structure of NaCl type. This is controversial since according to Sist *et al.*[72] this structural phase transition occurs at the lower temperature of 907 K. For SnSe, a second-order phase transition to the higher symmetry  $Cmcm$  phase occurs at  $T \sim 810$  K[73]. In the present work we consider only  $Pnma$  orthorhombic structures for both materials and thus report their transport properties for temperatures up to 807 and 900 K for SnSe and GeSe, respectively.

Both materials form covalently bonded layers with zig-zag chains along the b-axis and significant corrugation along the c-axis. Those layers are held together by much weaker van der Waals interactions along the out-of-plane a-axis. In order to capture such weak bonds between layers, we employed van der Waals corrections to DFT according to the D3 approach of Grimme *et al.* [74]. For GeSe, we started from the  $Pnma$  orthorhombic configuration from the Materials Project[75] (mp-700) and relaxed the lattice parameters and atomic positions until all atomic force components were smaller in magnitude than 1 meV/Å. The relaxed lattice constants are  $a = 11.02$  Å,  $b = 3.58$  Å and  $c = 4.79$  Å, which are in reasonable agreement with the corresponding experimental values[71, 76]. Importantly, our DFT-D3 calculations accurately reproduce the out-of-plane lattice constant (a-axis), differing from the experimental result at 919 K by only  $\sim 0.1\%$ . [71]

We used our Turbo-EPW implementation[49] to calculate the RTs limited by h-p coupling, including both contributions of nonpolar and screened polar scatterings. Turbo-EPW takes advantage of the dual interpolation technique based on a first Wannier-Fourier interpolation[77, 78], followed by a second interpolation using symmetry-adapted star functions, which allows for

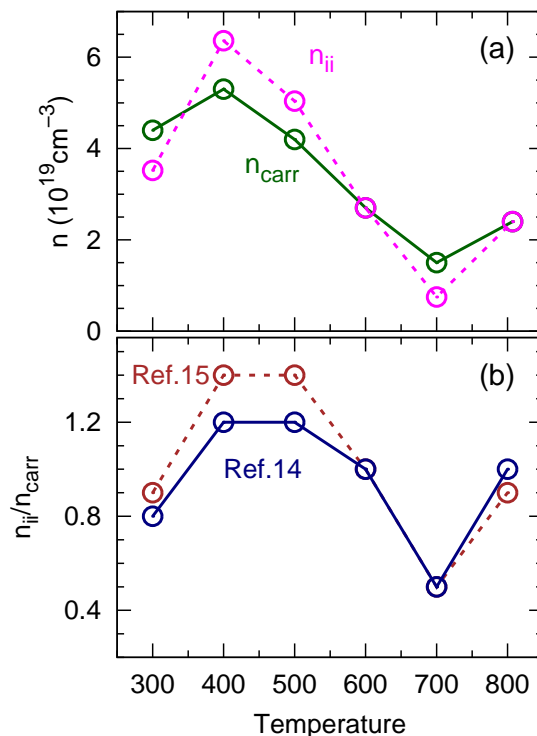


Figure 2: (a) Carrier density,  $n_{\text{carr}}$  (green solid line), and ionized impurity concentration,  $n_{\text{ii}}$  (dashed magenta line), determined by self-consistently matching calculations to the experimental results for a-axis p-doped SnSe reported in Zhao *et al.*[14]. (b) The ratio of values in (a),  $n_{\text{ii}}/n_{\text{carr}}$  (blue solid line), along with the same ratio as calculated in our previous work (brown dashed line) [28], derived from experimental results reported in Chang *et al.*[15] for the same axis.

efficient interpolation of h-p scattering matrix elements onto dense meshes of electron ( $\mathbf{k}$ ) and phonon ( $\mathbf{q}$ ) wave vectors. In the present case, the first interpolation, using maximally localized Wannier functions determined by Wannier90[79], leads to a phonon grid of  $10 \times 40 \times 20$   $\mathbf{q}$  points. The calculated electron self energy only changes by  $\sim 2\%$  for a ninefold denser  $\mathbf{q}$  grid, indicating that our momentum sampling gives a well converged balance between accuracy and computational cost. Subsequently,  $M = 10$  star functions per  $\mathbf{k}$  point were used for the second interpolation, resulting in a denser grid of  $27 \times 81 \times 64$   $\mathbf{k}$  points. In total this results in over 1 billion  $\mathbf{k}/\mathbf{q}$  pairs.

The calculation of  $\tau_{\text{imp}}$  requires the static and high-frequency dielectric constants,  $\zeta_0$  and  $\zeta_\infty$ . We have used the experimental values[80, 81]  $\zeta_0 = 21.9, 30.4, 25.8$  (45, 62, 42) and  $\zeta_\infty = 18.7, 21.9, 14.4$  (13, 17, 16) for the a-, b- and c-axis of GeSe (SnSe), respectively. We used the same value of  $M = 10$  star functions in the calculation of  $\tau_{\text{imp}}$  in order to obtain the same mesh for integration as in h-p calculations. Mathiessen's rule, Eq. (1), yields the temperature and energy dependent  $\tau_{\text{tot}}$  that is used in our modified BoltzTraP code[60, 61] to carry out transport calculations and determine all the TE properties.

## IV. Results and discussion

### A. Carrier density and ionized impurities concentration

The thermoelectric (TE) transport properties of GeSe depend on the carrier density,  $n_{\text{carr}}$ , and the concentration of ionized impurities,  $n_{\text{ii}}$ , both of which depend on the nonequilibrium growth process and can vary between samples. In order to make meaningful predictions we need to determine experimentally relevant values for  $n_{\text{carr}}$  and  $n_{\text{ii}}$ , including realistic temperature evolution. Due to the structural and chemical similarities between GeSe and SnSe, and the dearth of experimental data on GeSe, we use the carrier and impurity concentrations derived from SnSe experiments as a reasonable estimate for the values in GeSe samples. This has the added benefit of allowing direct comparison of TE properties of two materials that differ only in chemical composition.

Following the same procedure used in Ref. 60, we determine  $n_{\text{carr}}$  and  $n_{\text{ii}}$  by self-consistently adjusting their values in order to reproduce, within our computational framework, the experimentally measured values of  $S$  and  $\sigma$  in p-doped SnSe reported by Zhao *et al.*[14]. Even though the carrier density of SnSe presents only weak anisotropy, as inferred by Hall measurements on SnSe[13], we considered different  $n_{\text{carr}}$  for the in-plane and the out-

of-plane axes. We used the same temperature dependent  $n_{\text{carr}}$  and  $n_{\text{ii}}$  derived for p-doped SnSe to calculate TE transport properties of p-doped GeSe. For reasons of clarity, in the main text we report the results for a- and b-axis p-doped GeSe (referred to in the following as a-GeSe and b-GeSe, respectively) using  $n_{\text{carr}}$  and  $n_{\text{ii}}$  derived from a-axis p-doped SnSe. Results for c-axis GeSe (c-GeSe), as well as the properties calculated with  $n_{\text{carr}}$  and  $n_{\text{ii}}$  derived from b- or c-axis SnSe, are shown in Figures S1-S3. For reasons of expedience, we approximated  $n_{\text{carr}}$  and  $n_{\text{ii}}$  of GeSe at 800 K by the values obtained at 807 K for SnSe.

Figure 2(a) shows the carrier and impurity concentrations derived for a-axis p-doped SnSe as a function of  $T$ . The results derived for b- and c-axis p-doped SnSe are shown in the SM[53] (Figure S4). At 300 K  $n_{\text{carr}}$  is approximately  $4.4 \times 10^{19} \text{ cm}^{-3}$ , increases to  $5.3 \times 10^{19} \text{ cm}^{-3}$  at 400 K, and then decreases almost linearly down to  $1.5 \times 10^{19} \text{ cm}^{-3}$  at 700 K, all consistent with Hall measurements [14]. Above 700 K our results indicate that  $n_{\text{carr}}$  increases due to vacancy formation [28] reaching  $2.4 \times 10^{19} \text{ cm}^{-3}$  at 807 K. Figure 2(b) shows the temperature dependence of the ratio  $n_{\text{ii}}/n_{\text{carr}}$  compared to a previous calculation of the same quantity[28] that was based on the experimental data reported by Chang *et al.*[15] for a different a-axis SnSe sample with the same dopant. The similarity between the ratios determined in this work and those reported in our previous work demonstrates that these values of carrier and impurity concentrations are experimentally relevant and approximately sample independent.

## B. Thermoelectric transport properties

The calculated TE properties for p-doped out-of-plane (a-axis) and in-plane (b-axis) GeSe and SnSe are shown in Fig. 3, along with available experimental data[14]. All four systems show similar behavior of their Seebeck coefficients as a function of temperature, with  $S$  increasing with  $T$  up to 700 K, reaching  $332 \mu\text{V}/\text{K}$  ( $326 \mu\text{V}/\text{K}$ ) for a-GeSe (b-GeSe). Above that temperature the increase in  $n_{\text{carr}}$  causes  $S$  to decrease to  $319 \mu\text{V}/\text{K}$  ( $311 \mu\text{V}/\text{K}$ ) at 800 K. For temperatures above 600 K the calculated GeSe Seebeck coefficients are slightly higher than those of SnSe, in close agreement with previous theoretical findings. [46, 47] As pointed out by Hao *et al.*[47], p-doping in both materials induces a multiband effect that leads to an enhancement of  $S$ .

The electrical conductivity,  $\sigma$ , of all four systems shows the expected exponential decrease with temperature to 700 K, remaining nearly constant up to  $\sim 800$  K. Both axes of GeSe present  $\sigma$  values that are intermediate to those of a- and b-SnSe. As has been found previously, the in-plane electrical conductivity of GeSe is much lower than that of SnSe.[47] However, the out-of-plane  $\sigma$  of GeSe is greater than its in-plane  $\sigma$  and much higher than the out-of-plane conductivity in SnSe. This is a direct

consequence of the low scattering rate by ionized impurities for holes close to the valence band maximum (VBM) of a-GeSe, as will be discussed further below.

Similarly, the thermal conductivity due to hole transport,  $\kappa_{\text{h}}$ , also decreases with temperature up to 700 K and increases again for both materials between 700 and 800 K. The Lorenz function, defined as  $\Lambda = \kappa_{\text{h}}/(\sigma T)$ , is shown in Fig. 3(e), along with a red dashed line at the non-degenerate limit for semiconductors,  $\Lambda_{\text{nd}} = 2(k_B/e)^2 = 1.485 \times 10^{-8} \text{ V}^2 \text{ K}^{-2}$ . It has been shown previously that  $\Lambda$  can be much smaller than  $\Lambda_{\text{nd}}$  when a rigorous first-principles approach is used instead of simplified band structures and scattering processes [82, 83]. Both axes of GeSe have very small values of  $\Lambda$  that remain below  $\Lambda_{\text{nd}}$  throughout the temperature range. The Lorenz function for in-plane SnSe shows higher (lower) values than both axes of GeSe for temperatures below (above) 500 K. Even though a-SnSe also presents very low values of  $\Lambda$ , it is the highest of the four systems studied. Furthermore, it shows an abrupt enhancement above 700 K that is caused by a slight decrease in  $\sigma$  accompanied by a considerable increase in  $\kappa_{\text{h}}$ . Finally, the hole thermoelectric figure of merit,  $zT_{\text{h}} = S^2/\Lambda$ , is shown in Fig. 3(f).  $zT_{\text{h}}$  values are quite similar for both materials throughout the entire temperature range, except for a-SnSe that exhibits a sharp decrease at 800 K mirroring the increase in  $\Lambda$ .

## C. Dominant Scattering mechanisms and Relaxation times

In order to understand the temperature-dependent transport phenomena in GeSe and SnSe, we extensively analyzed their carrier scattering mechanisms. Figure 4 shows the relaxation times (RT) at 300 K due to nonpolar ( $\tau_{\text{npol}}$ ) and screened Fröhlich polar ( $\tau_{\text{pol}}$ ) scattering arising from the hole-phonon coupling, as well as scattering by ionized impurities ( $\tau_{\text{imp}}$ ) and the total RT ( $\tau_{\text{tot}}$ ) based on Mathiessen's rule, Eq. 1. These RTs are calculated as a function of the hole band and momentum, but plotted as a function of the hole energy using the following conversion:

$$\tau(\epsilon) = \frac{\sum_{n,\mathbf{k}} \tau_{n,\mathbf{k}} v_{n,\mathbf{k}} v_{n,\mathbf{k}} \delta(\epsilon - \epsilon_{n,\mathbf{k}})}{\sum_{n,\mathbf{k}} v_{n,\mathbf{k}} v_{n,\mathbf{k}} \delta(\epsilon - \epsilon_{n,\mathbf{k}})}. \quad (8)$$

In the SM[53] we provide additional details about the temperature dependence of the RTs as well as comparisons between the RTs for different systems and axes.

Due to the effectiveness of screening in these doped systems,  $\tau_{\text{pol}}$  is by far the largest RT, demonstrating that the Fröhlich coupling does not contribute significantly to the transport properties along either axis of p-doped GeSe. For both axes of GeSe we observe that  $\tau_{\text{imp}}$  is competitive with  $\tau_{\text{npol}}$  near the VBM at  $E = 0$ . For energies well below the VBM  $\tau_{\text{imp}}$  is quickly overtaken by  $\tau_{\text{npol}}$ . Comparing the results for the two axes in GeSe,

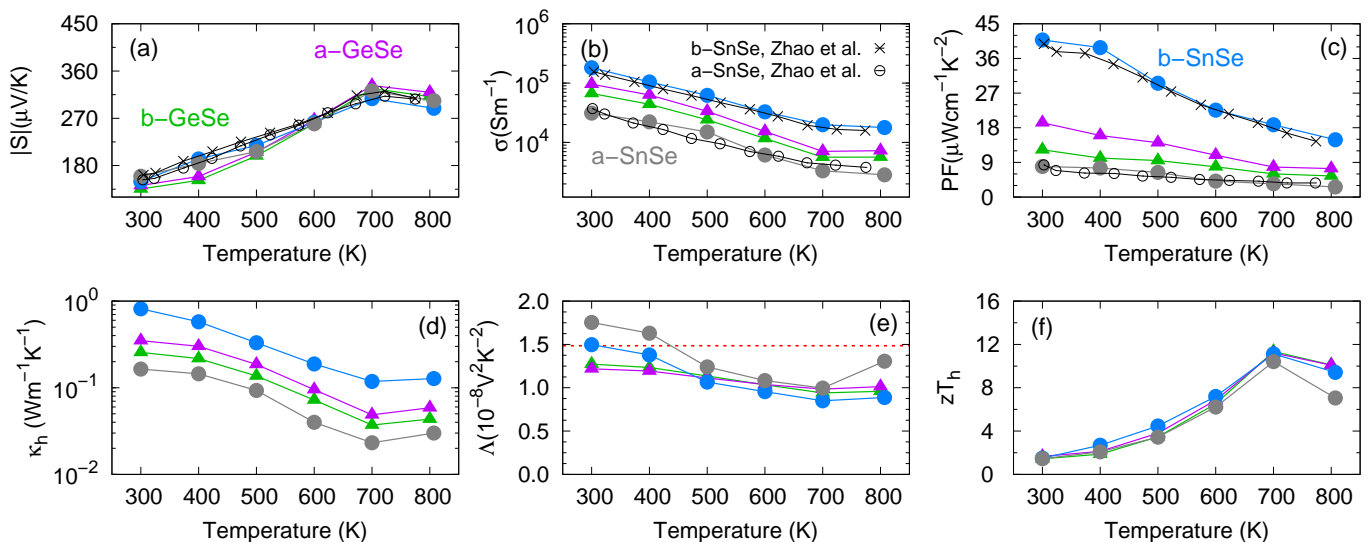


Figure 3: Calculated TE transport properties of p-doped GeSe and SnSe as functions of temperature, along with available experimental data on p-doped SnSe reported by Zhao *et al.*[14]. (a) Seebeck coefficient  $S$ , (b) electrical conductivity,  $\sigma$ , (c) power factor,  $PF$ , (d) thermal conductivity due to the hole transport,  $\kappa_h$ , (e) Lorenz function,  $\Lambda$ , with a dashed red line at  $\Lambda_{nd}$  (see text), and (f) the hole figure of merit,  $zT_h$ .

we observe the total RTs are quite similar in magnitude and present similar energetic behavior, as can also be clearly seen in Figure S5.

For SnSe the scenario is more complex because  $\tau_{npol}$  exhibits non-monotonic dependence on the hole energy with a minimum around  $E = -0.5$  eV. In this case,  $\tau_{imp}$  dominates the carrier scattering near the VBM for a-SnSe, while for b-SnSe  $\tau_{npol}$  and  $\tau_{imp}$  compete with each other.  $\tau_{npol}$  becomes dominant in the range of  $E = -0.8$  to  $-0.2$  eV, and the two mechanisms are comparable for lower energies. This complicated energy dependence of the RTs strongly affects the TE transport properties. In particular, it is responsible for the increase of  $\kappa_h$  at 807 K for a-SnSe, since the enhancement of  $\tau_{npol}$  and greater importance of scattering at higher energies increases the integral that appears in the calculation of  $\kappa_h$ [28]. A detailed comparison between the RTs for both axes in p-doped SnSe is presented in the SM[53] (Figs. S6, S7, S8 and S9), demonstrating that near the VBM  $\tau_{tot}$  is largely determined by  $\tau_{imp}$ . Thus, it is the higher  $\tau_{imp}$  that causes b-SnSe to have a larger  $\tau_{tot}$  than a-SnSe throughout the full range of temperatures studied.

By carefully comparing the total RTs of both materials, we observe that GeSe presents higher RT close to the VBM, which can be attributed mainly to the weaker scattering of holes by ionized impurities (see Figs. S6 and S10). Since all other contributions to  $\tau_{imp}$  are comparable in size, it must be the screening function  $F_{imp}$  that appears in the denominator of Eq. (S8) which leads to the larger RT. Hence, it is the greater effectiveness of the screening that raises the RT for GeSe. On the basis of Figures S10-S13 the use of SnSe RTs to estimate the thermoelectric figure of merit for GeSe cannot be justified, since we see that the SnSe RTs are generally

smaller near the VBM. Fig. S11 clearly shows that such an approximation would significantly underestimate the RT for a-GeSe. In addition, the clear variations in RT with hole energy is a strong argument against the use of the constant relaxation time approximation.

#### D. Average hole group velocities and Transport distribution function

The average hole group velocities as a function of energy can be derived from the calculated band structure:

$$v(\epsilon) = \sqrt{\frac{\sum_{n,\mathbf{k}} \left| \frac{\partial \epsilon_{n,\mathbf{k}}}{\partial \mathbf{k}} \right|^2 \delta(\epsilon - \epsilon_{n,\mathbf{k}})}{\sum_{n,\mathbf{k}} \delta(\epsilon - \epsilon_{n,\mathbf{k}})}}. \quad (9)$$

The group velocities, together with the energy dependent transport distribution function,  $\Sigma(\epsilon)$ , are shown in Fig. 5 for in-plane and out-of-plane GeSe and SnSe. Clearly, b-SnSe has the highest velocities around the VBM resulting in high electrical conductivity. Along the same line, the lowest velocities in a-SnSe are responsible for its inferior overall TE properties. Close to the VBM, GeSe presents intermediate values for  $v(\epsilon)$  and  $\Sigma(\epsilon)$ , higher than a-SnSe and lower than b-SnSe. Since the Seebeck coefficients of a-GeSe and b-GeSe are similar, it is the higher hole velocity, which leads to higher electrical conductivity, that results in the larger  $PF$  for a-GeSe. For GeSe, the velocities smoothly increase as hole energy increases away from the VBM, except for highly energetic holes in b-GeSe. On the other hand, for b-SnSe the velocities are high at the VBM, but they decrease with hole energy, becoming smaller than those of GeSe for holes between

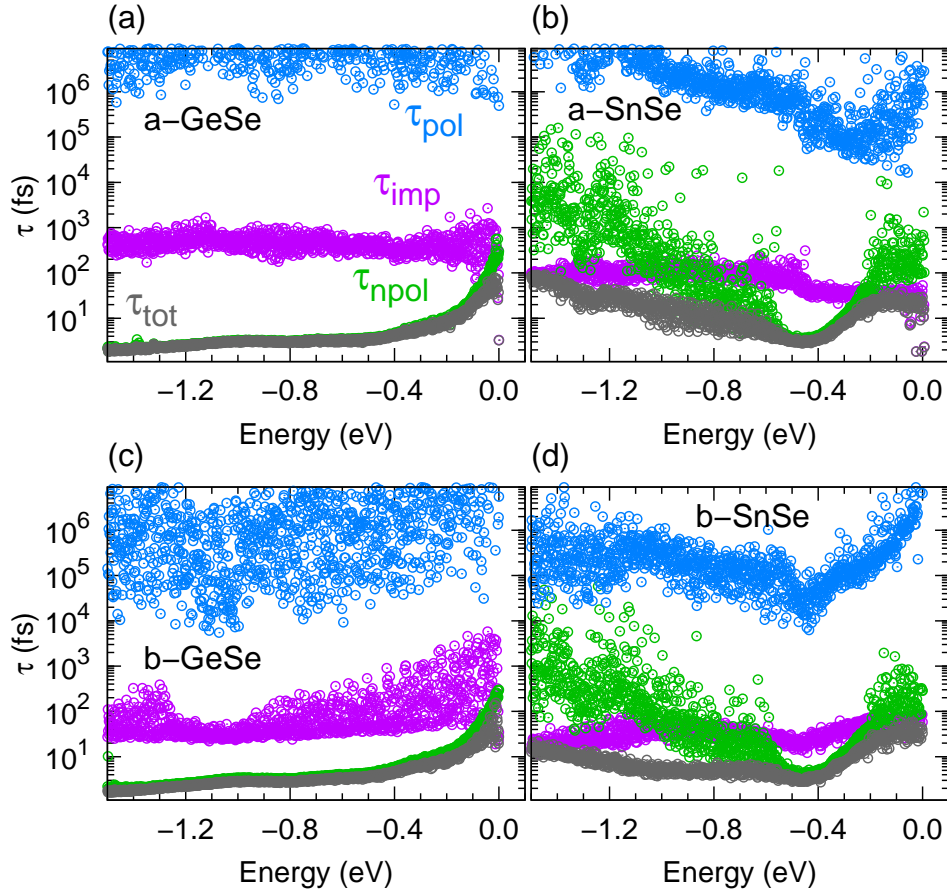


Figure 4: Relaxation times (RTs) at 300 K as a function of hole energy for (a) p-doped GeSe (a-axis), (b) p-doped SnSe (a-axis), (c) p-doped GeSe (b-axis) and (d) p-doped SnSe (b-axis). Each panel includes the screened Fröhlich polar scattering of optical phonons ( $\tau_{\text{pol}}$ , blue), nonpolar scattering of acoustic and optical phonons ( $\tau_{\text{npol}}$ , green), scattering by ionized impurities ( $\tau_{\text{imp}}$ , purple), and the total RT calculated with Mathiessen's rule ( $\tau_{\text{tot}}$ , grey). The zero of the energy scale corresponds to the VBM.

−0.3 eV to −0.6 eV. For GeSe, higher velocities at high hole energies contribute to the increase of  $\kappa_{\text{h}}$  between 700 and 800 K. In general, the behavior of  $\Sigma(\epsilon)$  follows that of the velocities.

### E. Outstanding thermoelectric performance of GeSe

In order to calculate the TE figure of merit,  $zT$ , we need an estimate of the total thermal conductivity,  $\kappa_{\text{tot}}$ . For SnSe we use the experimental values measured by Zhao *et al.*[14]. Since the necessary measurements have not yet been made for GeSe, we rely on theoretical results based on the Debye-Callaway theory for lattice thermal conductivity [47], to which we add our calculated hole thermal conductivities. The resulting total thermal conductivity for both SnSe and GeSe is plotted in Fig. S14. The thermal conductivity is nearly the same for a-axis GeSe and SnSe, though at the highest temperatures it is slightly lower for a-GeSe. In-plane b-GeSe exhibits higher total thermal conductivity than out-of-plane GeSe

throughout the temperature range, but it is comparatively lower than b-SnSe.

Both contributions to the total thermal conductivity are extremely low in GeSe. First, due to the relatively low electrical conductivity in GeSe and extremely low Lorenz numbers, carrier thermal conductivity is also very small. Second, GeSe displays strong anharmonicity as quantified by its large Grüneisen parameters that are comparable to or even larger than the Grüneisen parameters for SnSe [47]. Such anomalously high Grüneisen parameters of GeSe are a consequence of its hinge-like structure, distorted GeSe polyhedral, and van der Waals gaps in the out-of-plane direction that efficiently scatter phonons. Since the measured  $\kappa_{\text{tot}}$  for SnSe is extremely low, we expect the lattice contribution,  $\kappa_{\text{latt}}$ , to be extremely low for GeSe also.

In view of its relatively high Seebeck coefficients and extremely low Lorenz numbers, coupled with an ultralow  $\kappa_{\text{tot}}$ , we predict outstanding TE performance for out-of-plane GeSe, as can be seen in Fig. 6. In particular, a-GeSe has  $zT$  values that equal or even exceed the record-breaking performance of b-SnSe at temperatures above

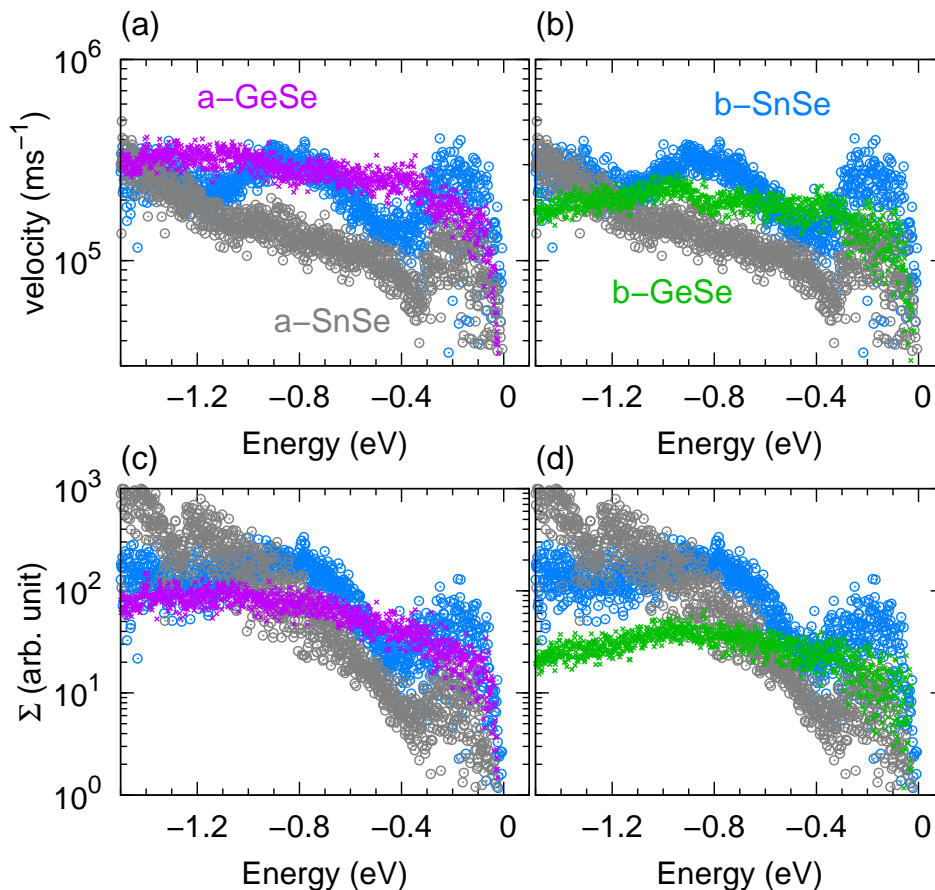


Figure 5: Average hole group velocity as a function of hole energy for (a) GeSe (a-axis, purple) and (b) GeSe (b-axis, green). Transport distribution function  $\Sigma$  at 300 K as a function of hole energy for (c) GeSe (a-axis, purple) and (d) GeSe (b-axis, green). For comparison, each panel shows the values for SnSe, a-axis (grey) and b-axis (blue).

500 K. This result would be missed if we assumed that the RTs for GeSe were the same as SnSe along the corresponding crystallographic axis. Along with a-GeSe, high TE performance has also been obtained for c-GeSe throughout the whole temperature range, while b-GeSe has comparatively lower TE performance. It is important to emphasize that GeSe, just like SnSe, presents high  $zT$  over a wide temperature range, which is a consequence of its relatively large band gap.[84] Furthermore, we continue to find a high figure of merit for out-of-plane GeSe when using  $n_{\text{carr}}$  and  $n_{\text{ii}}$  derived from b- and c-SnSe data (see Figures S15 and S16).

The figure of merit is increased for high power factors and low thermal conductivities. It is instructive to compare these contributions to  $zT$  for each of the systems studied here. For SnSe, the out-of-plane direction has a low power factor and a low thermal conductivity, and the former dominates, leading to a (relatively) low  $zT$  value. In contrast, the in-plane direction has a high power factor and a high thermal conductivity, and once again it is the power factor that dominates, this time yielding a high  $zT$  value. Compared to its SnSe counterpart, b-GeSe has much lower power factor as well as a somewhat

lower thermal conductivity, producing a comparably low  $zT$  value. The surprise, at least with reference to SnSe, is that a-GeSe maintains a very low  $\kappa_{\text{latt}}$  without the dramatic decrease in  $PF$  shown by a-SnSe.

It is important to note that the calculation of  $\kappa_{\text{latt}}$  is very challenging. For SnSe there is a long debate about  $\kappa_{\text{latt}}$  in the experimental literature[85–88] as well as questions regarding the comparison with first-principles calculations[86]. Similarly, the intrinsic thermal conductivity of GeSe is likely to be the subject of intense debate. Therefore, we re-calculated the value of  $zT$  for GeSe using values for  $\kappa_{\text{latt}}$  determined by Yuan et al.[89] based on third-order force constants. Their values of  $\kappa_{\text{latt}}$  are noticeably higher, leading to a lower prediction for  $zT$  as shown in the SM[53] (Figure S17). Even with the larger  $\kappa_{\text{latt}}$ , a-GeSe presents reasonable TE performance, reaching  $zT = 1.56$  at 800 K for  $n_{\text{carr}}$  and  $n_{\text{ii}}$  derived from a-SnSe. Though the approach of Yuan et al.[89] is more realistic than Debye-Callaway theory, the example of chalcogenides has shown that including additional factors such as thermal expansion, anharmonic phonon renormalization, four-phonon scattering, and impurity scatterings all generally serve to reduce the calculated



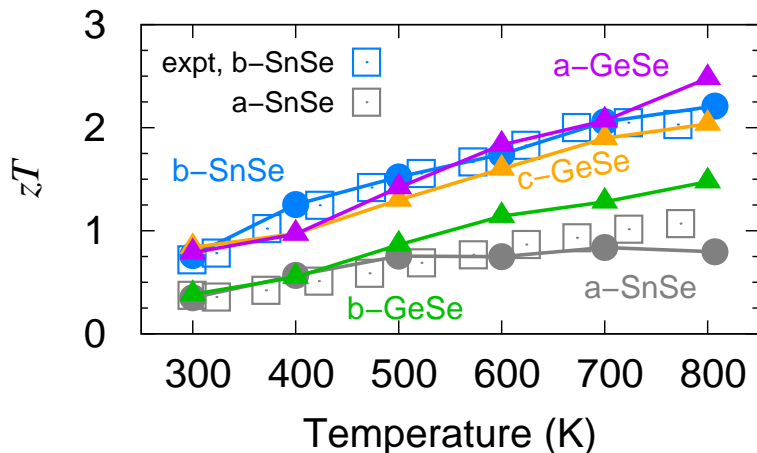


Figure 6: Thermoelectric figure of merit ( $zT$ ) as a function of temperature for p-doped a-GeSe (magenta), b-GeSe (green), c-GeSe (orange), a-SnSe (gray) and b-SnSe (blue). The experimental data reported by Zhao *et al.*[14] for both axes of p-doped SnSe are shown for comparison.

values of  $\kappa_{\text{latt}}$ [86, 90], bringing them closer to the simpler Debye-Callaway approximation. Since doped GeSe is a strongly anharmonic material, it is not unreasonable that the Debye-Callaway method might yield reasonable results, as it has for other low-conductivity thermoelectric compounds.[91]

Since GeSe should maintain its  $Pnma$  structure at higher temperatures than SnSe, we extend our analysis to 900 K. At that high temperature we estimate  $\kappa_{\text{latt}}$  using a  $1/T$  extrapolation [92] of the theoretical calculations done by Hao *et al.* [47] To that result we add  $\kappa_h$  calculated within our current framework. However, due to its phase transition, there is no SnSe transport data at 900 K that we can use to determine  $n_{\text{carr}}$  and  $n_{\text{ii}}$ . Instead, we scan over a range of  $n_{\text{carr}}$  and the ratio  $n_{\text{ii}}/n_{\text{carr}}$  and carry out transport calculations by solving the BTE for each pair of values. The density  $n_{\text{carr}}$  is varied between  $1 \times 10^{19} \text{ cm}^{-3}$  and  $10 \times 10^{19} \text{ cm}^{-3}$  in 10 equally spaced steps, while for each value of  $n_{\text{carr}}$ ,  $n_{\text{ii}}/n_{\text{carr}}$  was varied between 0.8 to 2.0 in steps of 0.2.

The calculated  $zT$  values along all three crystallographic axes of GeSe at 900 K are shown as a function of  $n_{\text{carr}}$  and  $n_{\text{ii}}/n_{\text{carr}}$  in Fig. 7. The out-of-plane direction presents the highest performance in comparison to the other axes, reaching the ultrahigh value of  $zT = 3.2$  at optimal  $n_{\text{carr}} = n_{\text{ii}} = 4 \times 10^{19} \text{ cm}^{-3}$ . It is important to note that  $zT$  remains very high even if the ratio  $n_{\text{ii}}/n_{\text{carr}}$  increases. For example,  $zT = 3.06$  when  $n_{\text{ii}}/n_{\text{carr}} = 2$ , indicating a high performance with  $zT$  larger than 3 even if  $n_{\text{ii}}$  is doubled. Horizontal line cuts at fixed ratios are shown in Fig. S18, clearly demonstrating that a tenfold increase in the ratio  $n_{\text{ii}}/n_{\text{carr}}$  can still lead to great performance provided  $n_{\text{carr}}$  is correspondingly increased. For example, with  $n_{\text{ii}}/n_{\text{carr}} = 10$ , an optimal value of  $n_{\text{carr}} = 6 \times 10^{19} \text{ cm}^{-3}$  yields  $zT = 2.7$ . Fig. S18 also shows the robustness of the high  $zT$  values as  $n_{\text{carr}}$  is varied. For instance,  $zT \geq 3$  for  $n_{\text{carr}}$  between  $3 \times 10^{19} \text{ cm}^{-3}$  and  $6 \times 10^{19} \text{ cm}^{-3}$  when  $n_{\text{ii}}/n_{\text{carr}} = 1$ . Though not as im-

pressive as the out-of-plane direction, the two in-plane directions still exhibit relatively high  $zT$  values at 900 K, namely,  $zT = 2.0$  (2.8) for the optimal ratio  $n_{\text{carr}} = n_{\text{ii}} = 5 \times 10^{19} \text{ cm}^{-3}$  for the b-axis (c-axis).

## V. Conclusions

In summary, we applied extensive first-principles calculations within the BTE framework to thoroughly investigate the temperature dependence of the TE transport properties of the orthorhombic  $Pnma$  phase of p-doped GeSe and SnSe. These calculations were done for values of the carrier density that yielded the record-breaking TE performance of p-doped SnSe.[14] We explicitly calculated the RTs due to nonpolar and screened Fröhlich polar h-p scattering, as well as the RT associated with the scattering by ionized impurities. The obtained temperature and hole-energy dependent RTs provide insight into the microscopic origin of the transport properties in p-doped GeSe and SnSe.

Our results indicate that the calculated GeSe Seebeck coefficients,  $S$ , are slightly higher than those of SnSe at temperatures above 600 K, while both axes of GeSe present electrical conductivity values that are intermediate between those of a- and b-SnSe. Importantly, both axes of GeSe exhibit Lorenz numbers below the non-degenerate limit of semiconductors. In-plane SnSe also has very low values for the Lorenz function  $\Lambda$ , and at temperatures above 500 K they are the same or even smaller than those of in-plane GeSe. On the other hand, a-SnSe possesses the highest  $\Lambda$  among all studied systems. Those results for  $\Lambda$  are directly correlated with TE performance, in which a low  $\Lambda$  plays a beneficial role in obtaining a high  $zT_h$ .

All axes of GeSe have quite low thermal conductivity  $\kappa_{\text{tot}}$ , which is a consequence of relatively low  $\sigma$  that yields low hole thermal conductivity, and high anhar-

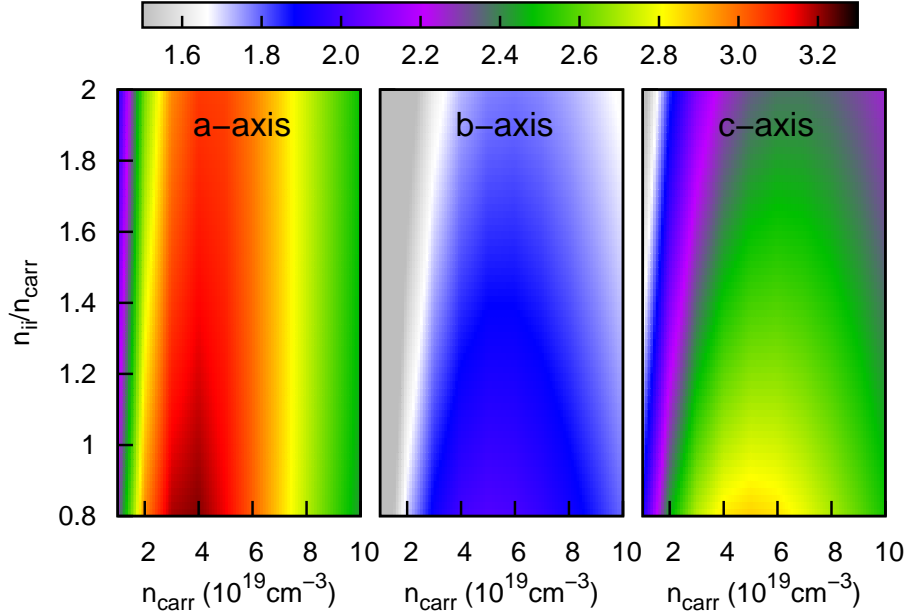


Figure 7: Colormap of the thermoelectric performance figure of merit  $zT$  as a function of the variation in  $n_{\text{carr}}$  and in the ratio  $n_{\text{ii}}/n_{\text{carr}}$  for out-of-plane (a-axis) and in-plane (b- and c-axis) GeSe at 900K.

monicity [47] that leads to predictions of low  $\kappa_{\text{latt}}$ . Combined with the high Seebeck coefficients, extremely low Lorenz numbers, and a relatively large band gap, our calculations predict an outstanding TE performance for both out-of-plane (a-axis) and in-plane (b- and c-axis) GeSe throughout a wide range of temperatures. Above 500 K the out-of-plane direction has  $zT$  values equal to or greater than the record-breaking performance of b-SnSe. By extending the analysis of the TE performance of GeSe to 900 K, we find that the out-of-plane direction still presents the highest performance compared to other axes, reaching an ultrahigh  $zT = 3.2$  at the optimal carrier density of  $4 \times 10^{19} \text{ cm}^{-3}$ . In addition, the two in-plane axes also have impressive figures of merit, with  $zT = 2.0$  (2.8) for the b-axis (c-axis) with optimal carrier density of  $5 \times 10^{19} \text{ cm}^{-3}$ . It is important to point out that the total RTs of out-of-plane GeSe are much higher than those of a-SnSe. Thus our results for the out-of-plane direction could not be anticipated by calculations using the same RTs as those for SnSe. [47]

Finally, it is also important to point out that intrinsic GeSe possesses low carrier density. To date Ge substitution by Ag is the most effective method of doping, enabling a hole density up to  $\sim 10^{18} \text{ cm}^{-3}$  and  $zT \approx 0.2$  at 700 K for polycrystalline GeSe. [48] This experimental result is far below our highest theoretically predicted value of  $zT = 3.2$  at 900 K, which can be attributed to the low carrier density that is far below our predicted optimal carrier density of  $\sim 10^{19} \text{ cm}^{-3}$ . Our results indicate that there is enormous room for further improvement in the TE performance of GeSe by increasing the doping to

optimal carrier density.

### Supplemental Material

Extra data and analyses are provided in the Supplemental Material.

### Conflicts of interest

There are no conflicts to declare.

### Acknowledgements

ASC and AA gratefully acknowledge support from the Brazilian agencies CNPq and FAPESP under Grants #2010/16970-0, #2013/08293-7, #2015/26434-2, #2016/23891-6, #2017/26105-4, and #2019/26088-8. DTL acknowledges funding from the STC Center for Integrated Quantum Materials, NSF Grant No. DMR-1231319; NSF DMREF Award No. 1922172; and the Army Research Office under Cooperative Agreement Number W911NF-21-2-0147. The calculations were performed at CCJDR-IFGW-UNICAMP in Brazil.

## Computer Code Availability

are available upon request.

All computer implementations of the methodology developed in this project were written in Fortran 90 and

- 
- [1] J. Mao, G. Chen, and Z. Ren, *Nature Materials*, **1** (2020).
- [2] J. Mao, H. Zhu, Z. Ding, Z. Liu, G. A. Gamage, G. Chen, and Z. Ren, *Science* **365**, 495 (2019).
- [3] F. J. DiSalvo, *Science* **285**, 703 (1999).
- [4] J. He and T. M. Tritt, *Science* **357**, eaak9997 (2017).
- [5] H. Lv, H. Liu, J. Shi, X. Tang, and C. Uher, *Journal of Materials Chemistry A* **1**, 6831 (2013).
- [6] R. Venkatasubramanian, E. Siivola, T. Colpitts, and B. O'quinn, *Nature* **413**, 597 (2001).
- [7] Y. Zhang, S. Hao, L.-D. Zhao, C. Wolverton, and Z. Zeng, *Journal of Materials Chemistry A* **4**, 12073 (2016).
- [8] B. Zhong, Y. Zhang, W. Li, Z. Chen, J. Cui, W. Li, Y. Xie, Q. Hao, and Q. He, *Applied Physics Letters* **105**, 123902 (2014).
- [9] M. Famili, I. M. Grace, Q. Al-Galiby, H. Sadeghi, and C. J. Lambert, *Advanced Functional Materials* **28**, 1703135 (2018).
- [10] Q. Xue, H. Liu, D. Fan, L. Cheng, B. Zhao, and J. Shi, *Physical Chemistry Chemical Physics* **18**, 17912 (2016).
- [11] H. Ohta, S. Kim, Y. Mune, T. Mizoguchi, K. Nomura, S. Ohta, T. Nomura, Y. Nakanishi, Y. Ikuhara, M. Hirano, H. Hosono, and K. Koumoto, *Nature Materials* **6**, 129 (2007).
- [12] T. Fu, X. Yue, H. Wu, C. Fu, T. Zhu, X. Liu, L. Hu, P. Ying, J. He, and X. Zhao, *Journal of Materiomics* **2**, 141 (2016).
- [13] L.-D. Zhao, S.-H. Lo, Y. Zhang, H. Sun, G. Tan, C. Uher, C. Wolverton, V. P. Dravid, and M. G. Kanatzidis, *Nature* **508**, 373 (2014).
- [14] L.-D. Zhao, G. Tan, S. Hao, J. He, Y. Pei, H. Chi, H. Wang, S. Gong, H. Xu, V. P. Dravid, C. Uher, G. J. Snyder, C. Wolverton, and M. G. Kanatzidis, *Science* **351**, 141 (2016).
- [15] C. Chang, M. Wu, D. He, Y. Pei, C.-F. Wu, X. Wu, H. Yu, F. Zhu, K. Wang, Y. Chen, L. Huang, J.-F. Li, J. He, and L.-D. Zhao, *Science* **360**, 778 (2018).
- [16] C. B. Vining, *Nature Materials* **8**, 83 (2009).
- [17] B. Sales, D. Mandrus, and R. K. Williams, *Science* **272**, 1325 (1996).
- [18] C. Zhou, Y. K. Lee, Y. Yu, S. Byun, Z.-Z. Luo, H. Lee, B. Ge, Y.-L. Lee, X. Chen, J. Y. Lee, C.-M. Oana, H. Chang, J. Im, S.-P. Cho, M. Wuttig, V. P. Dravid, M. G. Kanatzidis, and I. Chung, *Nature materials*, **1** (2021).
- [19] Y. Pei, X. Shi, A. LaLonde, H. Wang, L. Chen, and G. J. Snyder, *Nature* **473**, 66 (2011).
- [20] Y. Pei, H. Wang, and G. J. Snyder, *Advanced Materials* **24**, 6125 (2012).
- [21] A. M. Dehkordi, M. Zebarjadi, J. He, and T. M. Tritt, *Materials Science and Engineering: R: Reports* **97**, 1 (2015).
- [22] L.-D. Zhao, S. Hao, S.-H. Lo, C.-I. Wu, X. Zhou, Y. Lee, H. Li, K. Biswas, T. P. Hogan, C. Uher, C. Wolverton, V. P. Dravid, and K. M. G., *Journal of the American Chemical Society* **135**, 7364 (2013).
- [23] W. Liu, X. Tan, K. Yin, H. Liu, X. Tang, J. Shi, Q. Zhang, and C. Uher, *Physical Review Letters* **108**, 166601 (2012).
- [24] D. S. Parker, A. F. May, and D. J. Singh, *Physical Review Applied* **3**, 064003 (2015).
- [25] X. Chen, D. Parker, and D. J. Singh, *Scientific Reports* **3**, 3168 (2013).
- [26] R. L. González-Romero, A. Antonelli, A. S. Chaves, and J. J. Meléndez, *Physical Chemistry Chemical Physics* **20**, 1809 (2018).
- [27] R. W. McKinney, P. Gorai, V. Stevanović, and E. S. Toberer, *Journal of Materials Chemistry A* **5**, 17302 (2017).
- [28] A. S. Chaves, D. T. Larson, E. Kaxiras, and A. Antonelli, *Physical Review B* **104**, 115204 (2021).
- [29] A. I. Hochbaum, R. Chen, R. D. Delgado, W. Liang, E. C. Garnett, M. Najarian, A. Majumdar, and P. Yang, *Nature* **451**, 163 (2008).
- [30] A. I. Boukai, Y. Bunimovich, J. Tahir-Kheli, J.-K. Yu, W. A. Goddard III, and J. R. Heath, *Nature* **451**, 168 (2008).
- [31] M. G. Kanatzidis, *Chemistry of Materials* **22**, 648 (2009).
- [32] C. J. Vineis, A. Shakouri, A. Majumdar, and M. G. Kanatzidis, *Advanced Materials* **22**, 3970 (2010).
- [33] K. Biswas, J. He, I. D. Blum, C.-I. Wu, T. P. Hogan, D. N. Seidman, V. P. Dravid, and M. G. Kanatzidis, *Nature* **489**, 414 (2012).
- [34] H. Liu, X. Shi, F. Xu, L. Zhang, W. Zhang, L. Chen, Q. Li, C. Uher, T. Day, and G. J. Snyder, *Nature Materials* **11**, 422 (2012).
- [35] A. Olvera, N. Moroz, P. Sahoo, P. Ren, T. Bailey, A. Page, C. Uher, and P. Poudeu, *Energy & Environmental Science* **10**, 1668 (2017).
- [36] Y. Cheng, J. Yang, Q. Jiang, D. He, J. He, Y. Luo, D. Zhang, Z. Zhou, Y. Ren, and J. Xin, *Journal of Materials Chemistry A* **5**, 5163 (2017).
- [37] N. Ma, Y.-Y. Li, L. Chen, and L.-M. Wu, *Journal of the American Chemical Society* **142**, 5293 (2020).
- [38] S. Roychowdhury, T. Ghosh, R. Arora, M. Samanta, L. Xie, N. K. Singh, A. Soni, J. He, U. V. Waghmare, and K. Biswas, *Science* **371**, 722 (2021).
- [39] M. Taniguchi, R. Johnson, J. Ghijsen, and M. Cardona, *Physical Review B* **42**, 3634 (1990).
- [40] A. Okazaki, *Journal of the Physical Society of Japan* **13**, 1151 (1958).
- [41] P. D. Antunez, J. J. Buckley, and R. L. Brutchey, *Nanoscale* **3**, 2399 (2011).
- [42] S.-C. Liu, Y. Mi, D.-J. Xue, Y.-X. Chen, C. He, X. Liu, J.-S. Hu, and L.-J. Wan, *Advanced Electronic Materials* **3**, 1700141 (2017).
- [43] Z. Huang, S. A. Miller, B. Ge, M. Yan, S. Anand, T. Wu, P. Nan, Y. Zhu, W. Zhuang, G. J. Snyder, P. Jiang, and

- X. Bao, *Angewandte Chemie International Edition* **56**, 14113 (2017).
- [44] D. Sarkar, T. Ghosh, S. Roychowdhury, R. Arora, S. Sajan, G. Sheet, U. V. Waghmare, and K. Biswas, *Journal of the American Chemical Society* **142**, 12237 (2020).
- [45] D. Sarkar, S. Roychowdhury, R. Arora, T. Ghosh, A. Vasdev, B. Joseph, G. Sheet, U. V. Waghmare, and K. Biswas, *Angewandte Chemie* (2021).
- [46] G. Ding, G. Gao, and K. Yao, *Scientific reports* **5**, 1 (2015).
- [47] S. Hao, F. Shi, V. P. Dravid, M. G. Kanatzidis, and C. Wolverton, *Chemistry of Materials* **28**, 3218 (2016).
- [48] X. Zhang, J. Shen, S. Lin, J. Li, Z. Chen, W. Li, and Y. Pei, *Journal of Materiomics* **2**, 331 (2016).
- [49] A. S. Chaves, A. Antonelli, D. T. Larson, and E. Kaxiras, *Physical Review B* **102**, 125116 (2020).
- [50] P. Hohenberg and W. Kohn, *Physical Review* **136**, B864 (1964).
- [51] W. Kohn and L. J. Sham, *Physical Review* **140**, A1133 (1965).
- [52] S. Baroni, S. De Gironcoli, A. Dal Corso, and P. Giannozzi, *Reviews of Modern Physics* **73**, 515 (2001).
- [53] See Supplemental Material (SM) at for a more comprehensive theoretical framework, additional details about the temperature dependence of the relaxation times (RTs), comparisons between the RTs for different systems and axes, additional analysis of the carrier densities, concentration of ionized impurities and thermoelectric figure of merit for different axes and conditions. SM contains additional references [93-101].
- [54] C. Pellegrini, A. Marinelli, and S. Reiche, *Reviews of Modern Physics* **88**, 015006 (2016).
- [55] C. Bostedt, S. Boutet, D. M. Fritz, Z. Huang, H. J. Lee, H. T. Lemke, A. Robert, W. F. Schlotter, J. J. Turner, and G. J. Williams, *Reviews of Modern Physics* **88**, 015007 (2016).
- [56] P. Vogl, *Physical Review B* **13**, 694 (1976).
- [57] H. Ehrenreich, *Journal of Physics and Chemistry of Solids* **8**, 130 (1959).
- [58] H. Brooks, in *Advances in electronics and electron physics*, Vol. 7 (Elsevier, 1955) pp. 85–182.
- [59] D. Chattopadhyay and H. Queisser, *Reviews of Modern Physics* **53**, 745 (1981).
- [60] A. S. Chaves, R. L. González-Romero, J. J. Meléndez, and A. Antonelli, *Physical Chemistry Chemical Physics* **23**, 900 (2021).
- [61] G. K. Madsen and D. J. Singh, *Computer Physics Communications* **175**, 67 (2006).
- [62] P. Giannozzi, S. Baroni, N. Bonini, M. Calandra, R. Car, C. Cavazzoni, D. Ceresoli, G. L. Chiarotti, M. Cococcioni, I. Dabo, A. Dal Corso, S. de Gironcoli, S. Fabris, G. Fratesi, R. Gebauer, U. Gerstmann, C. Gougoussis, A. Kokalj, M. Lazzeri, L. Martin-Samos, N. Marzari, F. Mauri, R. Mazzarello, S. Paolini, A. Pasquarello, L. Paulatto, C. Sbraccia, S. Scandolo, G. Sclauzero, A. P. Seitsonen, A. Smogunov, P. Umari, and R. M. Wentzcovitch, *Journal of Physics: Condensed Matter* **21**, 395502 (2009).
- [63] D. Hamann, *Physical Review B* **88**, 085117 (2013).
- [64] M. Van Setten, M. Giantomassi, E. Bousquet, M. J. Verstraete, D. R. Hamann, X. Gonze, and G.-M. Rignanese, *Computer Physics Communications* **226**, 39 (2018).
- [65] J. P. Perdew, K. Burke, and M. Ernzerhof, *Physical Review Letters* **77**, 3865 (1996).
- [66] A. Elkorashy, *physica status solidi (b)* **152**, 249 (1989).
- [67] D. D. Vaughn, R. J. Patel, M. A. Hickner, and R. E. Schaak, *Journal of the American Chemical Society* **132**, 15170 (2010).
- [68] L. Ross and M. Bourgon, *Canadian Journal of Chemistry* **47**, 2555 (1969).
- [69] H. Ipser, M. Gambino, and W. Schuster, *Monatshefte für Chemie/Chemical Monthly* **113**, 389 (1982).
- [70] D. Bletskan, *Journal of Ovonic Research* **1**, 53 (2005).
- [71] H. Wiedemeier and P. Siemers, *Zeitschrift für anorganische und allgemeine Chemie* **411**, 90 (1975).
- [72] M. Sist, C. Gatti, P. Nørby, S. Cenedese, H. Kasai, K. Kato, and B. B. Iversen, *Chemistry—A European Journal* **23**, 6888 (2017).
- [73] C. W. Li, J. Hong, A. F. May, D. Bansal, S. Chi, T. Hong, G. Ehlers, and O. Delaire, *Nature Physics* **11**, 1063 (2015).
- [74] S. Grimme, J. Antony, S. Ehrlich, and H. Krieg, *The Journal of Chemical Physics* **132**, 154104 (2010).
- [75] A. Jain, S. P. Ong, G. Hautier, W. Chen, W. D. Richards, S. Dacek, S. Cholia, D. Gunter, D. Skinner, G. Ceder, and K. A. Persson, *APL materials* **1**, 011002 (2013).
- [76] H. Wiedemeier and H. G. von Schnering, *Z. Kristallogr* **148**, 3 (1978).
- [77] F. Giustino, M. L. Cohen, and S. G. Louie, *Physical Review B* **76**, 165108 (2007).
- [78] S. Poncé, E. R. Margine, C. Verdi, and F. Giustino, *Computer Physics Communications* **209**, 116 (2016).
- [79] A. A. Mostofi, J. R. Yates, Y.-S. Lee, I. Souza, D. Vanderbilt, and N. Marzari, *Computer Physics Communications* **178**, 685 (2008).
- [80] O. Madelung, *Semiconductors: data handbook* (Springer Science & Business Media, 2004).
- [81] H. Chandrasekhar, R. Humphreys, U. Zwick, and M. Cardona, *Physical Review B* **15**, 2177 (1977).
- [82] X. Wang, V. Askarpour, J. Maassen, and M. Lundstrom, *Journal of Applied Physics* **123**, 055104 (2018).
- [83] A. Putatunda and D. J. Singh, *Materials Today Physics* **8**, 49 (2019).
- [84] Y. Xiao and L.-D. Zhao, *Science* **367**, 1196 (2020).
- [85] P.-C. Wei, S. Bhattacharya, J. He, S. Neeleshwar, R. Podila, Y. Chen, and A. Rao, *Nature* **539**, E1 (2016).
- [86] D. Wu, L. Wu, D. He, L.-D. Zhao, W. Li, M. Wu, M. Jin, J. Xu, J. Jiang, L. Huang, Y. Zhu, M. G. Kanatzidis, and J. He, *Nano Energy* **35**, 321 (2017).
- [87] G. Li, U. Aydemir, M. Wood, W. A. Goddard III, P. Zhai, Q. Zhang, and G. J. Snyder, *Chemistry of Materials* **29**, 2382 (2017).
- [88] Y.-X. Chen, Z.-H. Ge, M. Yin, D. Feng, X.-Q. Huang, W. Zhao, and J. He, *Advanced Functional Materials* **26**, 6836 (2016).
- [89] K. Yuan, Z. Sun, X. Zhang, and D. Tang, *Scientific reports* **9**, 1 (2019).
- [90] Y. Xia, *Applied Physics Letters* **113**, 073901 (2018).
- [91] Y. Zhang, E. Skoug, J. Cain, V. Ozoliņš, D. Morelli, and C. Wolverton, *Physical Review B* **85**, 054306 (2012).
- [92] G. Grimvall, *Thermophysical Properties of Materials* (Elsevier, 1999).
- [93] F. Giustino, *Reviews of Modern Physics* **89**, 015003 (2017).
- [94] S. Poncé, E. R. Margine, and F. Giustino, *Physical Review B* **97**, 121201 (2018).

- [95] S. Poncé, W. Li, S. Reichardt, and F. Giustino, Reports on Progress in Physics **83**, 036501 (2020).
- [96] H. Fröhlich, Proc. Roy. Soc.(London) **160**, 230 (1937).
- [97] C. Verdi and F. Giustino, Physical Review Letters **115**, 176401 (2015).
- [98] N. Marzari and D. Vanderbilt, Physical review B **56**, 12847 (1997).
- [99] B. M. Askerov and S. Figarova, *Thermodynamics, Gibbs Method and Statistical Physics of Electron Gases*, Vol. 57 (Springer Science & Business Media, 2009).
- [100] D. G. Shankland, in *Computational Methods in Band Theory* (Springer, 1971) pp. 362–367.
- [101] D. Koelling and J. Wood, Journal of Computational Physics **67**, 253 (1986).

## Supplementary Information: Outstanding thermoelectric performance predicted for out-of-plane p-doped GeSe

Anderson S. Chaves,<sup>1,2</sup> Daniel T. Larson,<sup>3</sup> Efthimios Kaxiras,<sup>3,2</sup> and Alex Antonelli<sup>4</sup>

<sup>1</sup>*Gleb Wataghin Institute of Physics, University of Campinas, PO Box 13083-859, Campinas, SP, Brazil*

<sup>2</sup>*John A. Paulson School of Engineering and Applied Sciences,  
Harvard University, Cambridge, Massachusetts, 02138, USA*

<sup>3</sup>*Department of Physics, Harvard University, Cambridge, Massachusetts, 02138, USA*

<sup>4</sup>*Gleb Wataghin Institute of Physics and Center for Computing in Engineering & Sciences,  
University of Campinas, PO Box 13083-859, Campinas, SP, Brazil*

(Dated: February 15, 2022)

## I. Details of the theoretical framework

The hole-phonon (h-p) relaxation time (RT) is directly related to the imaginary part of the momentum- and band-resolved Fan-Migdal electron self-energy[1–3],  $1/\tau_{n,\mathbf{k}} = 2 \text{Im } \Theta_{n,\mathbf{k}}(\epsilon = 0, T)$ , where

$$\begin{aligned} \text{Im } \Theta_{n,\mathbf{k}}(\epsilon, T) &= \pi \sum_{m,\theta} \int_{BZ} \frac{d\mathbf{q}}{\Omega_{BZ}} |g_{mn,\theta}(\mathbf{k}, \mathbf{q})|^2 \\ &\times \left[ [n_{\mathbf{q}\theta}(T) + f_{m\mathbf{k}+\mathbf{q}}] \delta(\epsilon - (\epsilon_{m\mathbf{k}+\mathbf{q}} - \epsilon_F) + \omega_{\mathbf{q}\theta}) \right. \\ &\left. + [n_{\mathbf{q}\theta}(T) + 1 - f_{m\mathbf{k}+\mathbf{q}}] \delta(\epsilon - (\epsilon_{m\mathbf{k}+\mathbf{q}} - \epsilon_F) - \omega_{\mathbf{q}\theta}) \right], \end{aligned} \quad (1)$$

$\epsilon_F$  is the Fermi energy calculated by DFT at 0K,  $g_{mn,\theta}(\mathbf{k}, \mathbf{q}) = \langle \Psi_{m\mathbf{k}+\mathbf{q}} | \partial_{\mathbf{q}\theta} V_{KS}(r) | \Psi_{n\mathbf{k}} \rangle$  are the h-p coupling matrix elements that are calculated within DFPT,  $|\Psi_{n\mathbf{k}}\rangle$  are Kohn-Sham (KS) orbitals and  $\partial_{\mathbf{q}\theta} V_{KS}$  corresponds to the change of the KS potential upon a vibrational perturbation with momentum  $\mathbf{q}$  and branch index  $\theta$ ,  $\omega_{\mathbf{q}\theta}$  are the corresponding phonon eigenfrequencies,  $n_{\mathbf{q}\theta}(T)$  is the Bose-Einstein distribution,  $\epsilon_{m\mathbf{k}}$  is the KS energy of a hole in band  $m$  with momentum  $\mathbf{k}$ ,  $f_{m\mathbf{k}+\mathbf{q}}$  is the Fermi-Dirac distribution, and  $\Omega_{BZ}$  is the volume of the Brillouin zone (BZ).

For polar materials, such as GeSe and SnSe, holes can be scattered by a multipolar electric polarization caused by longitudinal optical (LO) phonons and described by the Fröhlich coupling [4]. We employ a first-principles approach to the Fröhlich coupling[5] which allows for an analytical treatment of the long-range polar singularity. To accomplish this, the h-p matrix element is separated into short-range ( $g_{mn,\theta}^S$ ) and long-range ( $g_{mn,\theta}^L$ ) parts. The  $S$  part is well behaved and is amenable to W-F interpolation. On the other hand, the  $L$  part is determined analytically using the Vogl formula [6–8]:

$$\begin{aligned} g_{mn,\theta}^L(\mathbf{k}, \mathbf{q}) &= i \frac{e^2}{\Omega \epsilon_0} \sum_{\kappa} \left( \frac{\hbar}{2NM_{\kappa}\omega_{\mathbf{q}\theta}} \right)^{\frac{1}{2}} \\ &\times \sum_{\mathbf{G} \neq -\mathbf{q}} \frac{(\mathbf{q} + \mathbf{G}) \cdot \mathbf{Z}_{\kappa}^* \cdot \mathbf{e}_{\kappa\theta}(\mathbf{q})}{(\mathbf{q} + \mathbf{G}) \cdot \boldsymbol{\zeta}_{\infty} \cdot (\mathbf{q} + \mathbf{G})} \\ &\times \langle \Psi_{m\mathbf{k}+\mathbf{q}} | e^{i(\mathbf{k}+\mathbf{q}) \cdot \mathbf{r}} | \Psi_{n\mathbf{k}} \rangle. \end{aligned} \quad (2)$$

Here  $\langle \Psi_{m\mathbf{k}+\mathbf{q}} | e^{i(\mathbf{k}+\mathbf{q}) \cdot \mathbf{r}} | \Psi_{n\mathbf{k}} \rangle = [U_{\mathbf{k}+\mathbf{q}} U_{\mathbf{k}}^+]_{mn}$  are phase factors given in terms of rotation matrices,  $U_{\mathbf{k}+\mathbf{q}}$ , that appear in the definition of maximally localized Wannier functions (MLWFs).[9]  $\Omega$  is the volume of the unit cell,  $M_{\kappa}$  corresponds to the mass of atom  $\kappa$ ,  $N$  is the number of unit cells in the Born-von Kármán supercell,  $\mathbf{G}$  is a reciprocal lattice vector,  $\mathbf{Z}^* = Z_{\alpha,\beta}^*$  is the Born effective charge tensor,  $\mathbf{e}_{\kappa\theta}(\mathbf{q})$  is a phonon eigenmode normalized within the unit cell,  $\boldsymbol{\zeta}_{\infty} = \zeta_{\alpha,\beta}^{\infty}$  corresponds to the high-frequency dielectric constant tensor,  $\epsilon_0$  is the vacuum permittivity,  $\hbar$  is the reduced Planck constant, and  $e$  is the absolute electron charge.

By using the quasi-static Ehrenreich theory [10] and following Ref. 11, we generalize the first-principles approach to the Fröhlich coupling by including screening effects due to free carriers in the material that efficiently screen out the electric field produced by optical vibrations. This is accomplished by dividing the RT by the following band-dependent screening factor:

$$F_{\text{pol}}(n, \mathbf{k}) = \left[ 1 - \frac{1}{2(r_{\infty}(n, \mathbf{k}) \cdot \mathbf{k})^2} \ln[1 + 4(r_{\infty}(n, \mathbf{k}) \cdot \mathbf{k})^2] + \frac{1}{1 + 4(r_{\infty}(n, \mathbf{k}) \cdot \mathbf{k})^2} \right]^{-1}, \quad (3)$$

where  $r_{\infty}$  is the screening radius given by

$$r_{\infty}^{-2}(n, \mathbf{k}) = \frac{4\pi e^2}{\zeta_{\infty}} \int \left( -\frac{\partial f_{\mu}(T, \epsilon)}{\partial \epsilon_{n,\mathbf{k}}} \right) g(\epsilon) d\epsilon. \quad (4)$$

Here  $g(\epsilon)$  is the density of states (DOS), which can be evaluated over an energy grid with spacing  $d\epsilon$  as follows:

$$g(\epsilon) = \int \sum_n \delta(\epsilon - \epsilon_{n,\mathbf{k}}) \frac{d\mathbf{k}}{8\pi^3} = \frac{1}{\Omega N_{\mathbf{k}}} \sum_{n,\mathbf{k}} \frac{\delta(\epsilon - \epsilon_{n,\mathbf{k}})}{d\epsilon}, \quad (5)$$

where  $N_{\mathbf{k}}$  the number of  $\mathbf{k}$  points sampled. Thus from Eqs. 1, 2, and 3 we arrive at the final expressions for the RTs due to nonpolar ( $\tau_{\text{npol}}$ ) and screened polar ( $\tau_{\text{pol}}$ ) scattering:

$$\frac{1}{\tau_{\text{npol}}} \equiv \frac{1}{\tau_{n,\mathbf{k}}^{\text{npol}}} = 2 \text{Im} \Theta_{n,\mathbf{k}}[\epsilon = 0, T, g_{mn,\theta}^S(\mathbf{k}, \mathbf{q})], \quad (6)$$

$$\frac{1}{\tau_{\text{pol}}} \equiv \frac{1}{\tau_{n,\mathbf{k}}^{\text{pol}}} = 2 \text{Im} \Theta_{n,\mathbf{k}}[\epsilon = 0, T, g_{mn,\theta}^{\mathcal{L}}(\mathbf{k}, \mathbf{q})] \times F_{\text{pol}}(n, \mathbf{k}). \quad (7)$$

Extrinsic scattering by ionized impurities is included using the theory developed by Brooks and Herring (B-H).[12, 13] Following Refs. 14, 15, and 11, the RT due to the scattering of holes by ionized impurities can be written as

$$\tau_{\text{imp}} \equiv \tau^{\text{imp}}(n, \mathbf{k}) = \frac{\hbar \zeta_0^2}{2\pi e^4 n_{\text{ii}} F_{\text{imp}}(n, \mathbf{k})} \mathbf{k}^2 \left| \frac{\partial \epsilon_{n,\mathbf{k}}}{\partial \mathbf{k}} \right|, \quad (8)$$

where  $n_{\text{ii}}$  is the concentration of ionized impurities,

$$F_{\text{imp}}(n, \mathbf{k}) = \ln(1 + \eta) - \frac{\eta}{1 + \eta} \quad (9)$$

is the screening function, with  $\eta = (2\mathbf{k} \cdot r_0(n, \mathbf{k}))^2$ , and the static screening radius  $r_0$  is given by Eq. 4, now screened by the static dielectric constant,  $\zeta_0$ . It is important to note that the expression above for  $\tau_{\text{imp}}$  extends the parabolic band approximation in such a way that the average electronic group velocities in the expression are given analytically in terms of Fourier interpolation of the DFT band structure through star functions[14, 16–18]. Namely,

$$\frac{\partial \epsilon_{n,\mathbf{k}}}{\partial \mathbf{k}} \equiv v(n, \mathbf{k}) \approx \frac{i}{n_s} \sum_{m=1}^M a_m \sum_{\{s\}} (s\mathbf{R}_m) \exp[i(s\mathbf{R}_m) \cdot \mathbf{k}], \quad (10)$$

with the sum running over all  $n_s$  point group symmetry operations  $\{s\}$  acting on the direct lattice  $\mathbf{R}_m$ . Here  $M$  is the number of star functions per  $\mathbf{k}$  point and  $a_m$  are the Fourier coefficients of the expansion of the band structure in terms of star functions.



## II. Additional figures

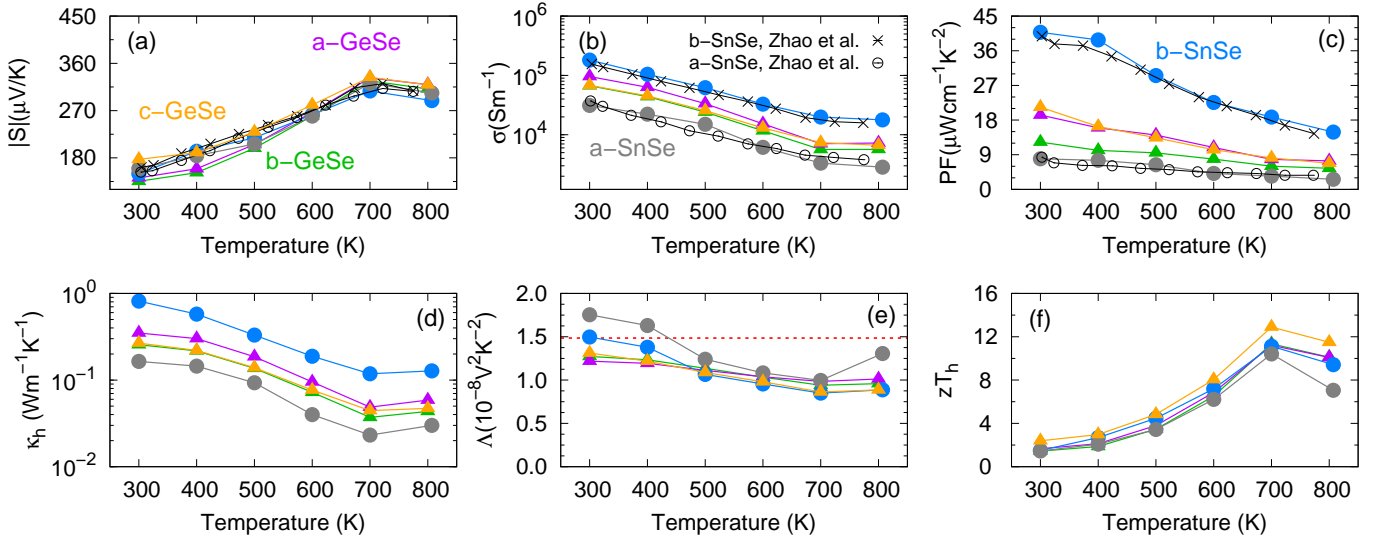


Fig. S1. The same as Fig. 3 but including c-GeSe. Calculated thermoelectric transport properties of p-doped GeSe (all axes) and SnSe (a- and b-axis) as functions of temperature, along with available experimental data on p-doped SnSe reported by Zhao *et al.*[19]. The GeSe transport properties were calculated by using the temperature dependent carrier density and the ionized impurities concentrations derived from a-axis p-doped SnSe, also reported by Zhao *et al.*[19]. (a) Seebeck coefficient  $S$ , (b) electrical conductivity,  $\sigma$ , (c) power factor, PF, (d) thermal conductivity due to the hole transport,  $\kappa_h$ , (e) Lorenz function,  $\Lambda$ , where the horizontal dashed red line indicates the non-degenerate limit for semiconductors,  $\Lambda_{nd} = 1.485 \times 10^{-8} \text{V}^2 \text{K}^{-2}$ , and (f) the hole figure of merit,  $zT_h$ .

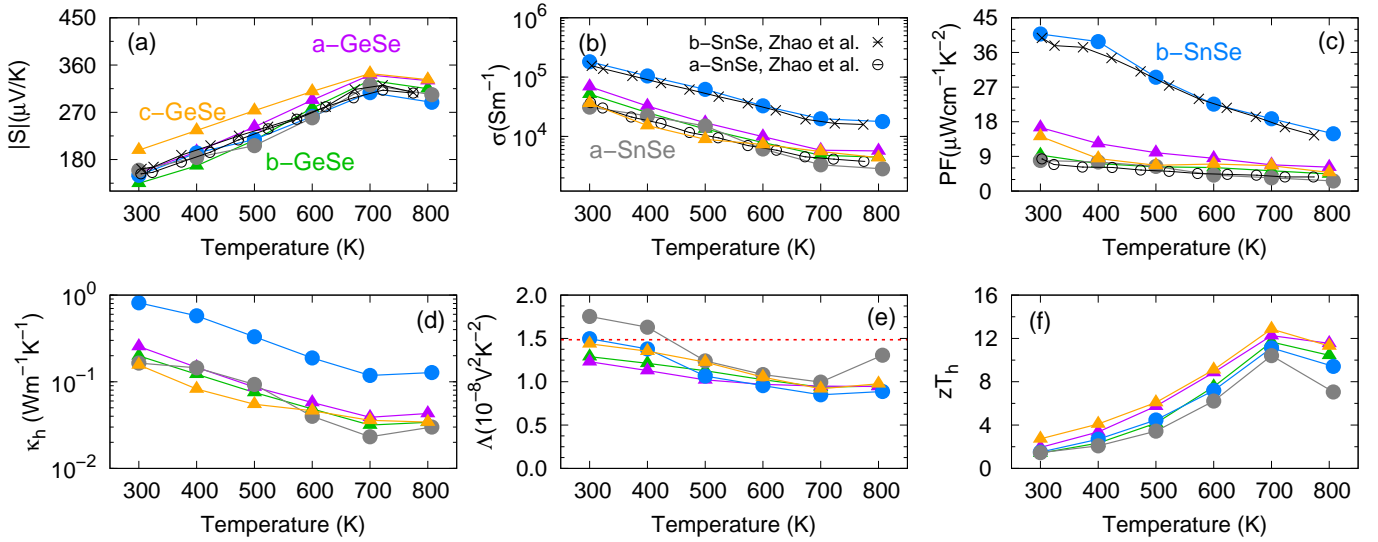


Fig. S2. Calculated thermoelectric transport properties of p-doped GeSe (all axes) and SnSe (a- and b-axis) as functions of temperature, along with available experimental data on p-doped SnSe reported by Zhao *et al.*[19] The GeSe transport properties were calculated by using the temperature dependent carrier density and the ionized impurities concentrations derived from b-axis p-doped SnSe, also reported by Zhao *et al.*[19] (a) Seebeck coefficient  $S$ , (b) electrical conductivity,  $\sigma$ , (c) power factor, PF, (d) thermal conductivity due to the hole transport,  $\kappa_h$ , (e) Lorenz function,  $\Lambda$ , where the horizontal dashed red line indicates the non-degenerate limit for semiconductors,  $\Lambda_{nd} = 1.485 \times 10^{-8} \text{V}^2 \text{K}^{-2}$ , and (f) the hole figure of merit,  $zT_h$ .

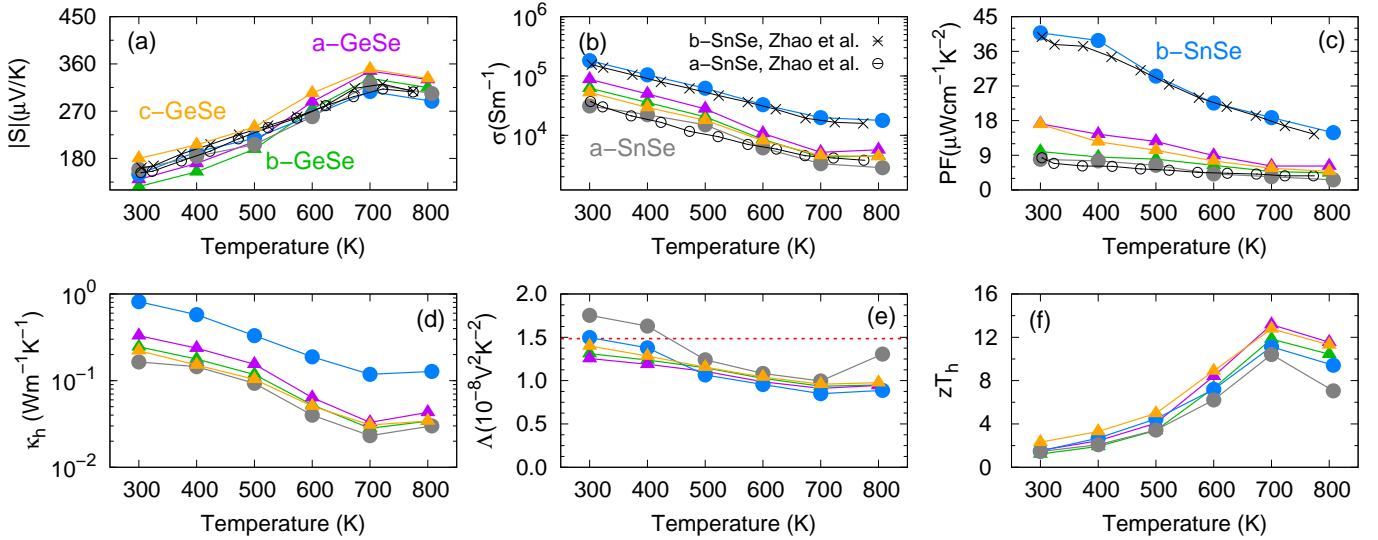


Fig. S3. Calculated thermoelectric transport properties of p-doped GeSe (all axes) and SnSe (a- and b-axis) as functions of temperature, along with available experimental data on p-doped SnSe reported by Zhao *et al.*[19] The GeSe transport properties were calculated by using the temperature dependent carrier density and the ionized impurities concentrations derived from c-axis p-doped SnSe, also reported by Zhao *et al.*[19] (a) Seebeck coefficient  $S$ , (b) electrical conductivity,  $\sigma$ , (c) power factor, PF, (d) thermal conductivity due to the hole transport,  $\kappa_h$ , (e) Lorenz function,  $\Lambda$ , where the horizontal dashed red line indicates the non-degenerate limit for semiconductors,  $\Lambda_{nd} = 1.485 \times 10^{-8} \text{V}^2 \text{K}^{-2}$ , and (f) the hole figure of merit,  $zT_h$ .

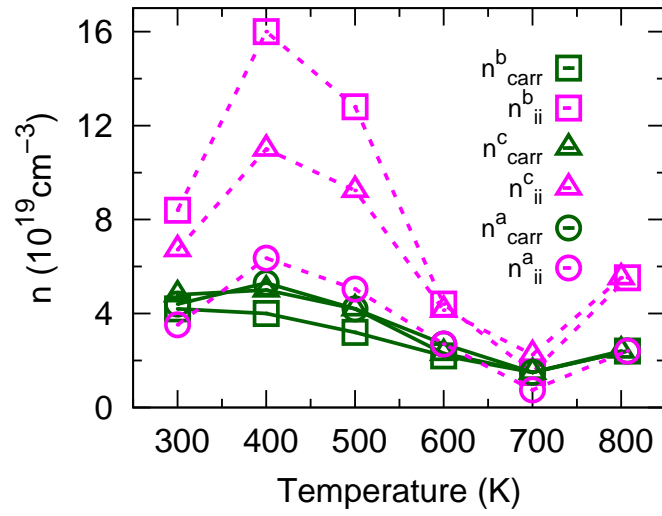


Fig. S4. Carrier density,  $n_{\text{carr}}$  (green solid line), and ionized impurity concentration,  $n_{\text{ii}}$  (dashed magenta line), determined by self-consistently matching the experimental results for a-, b- and c-axis p-doped SnSe reported in Zhao et al.[19]

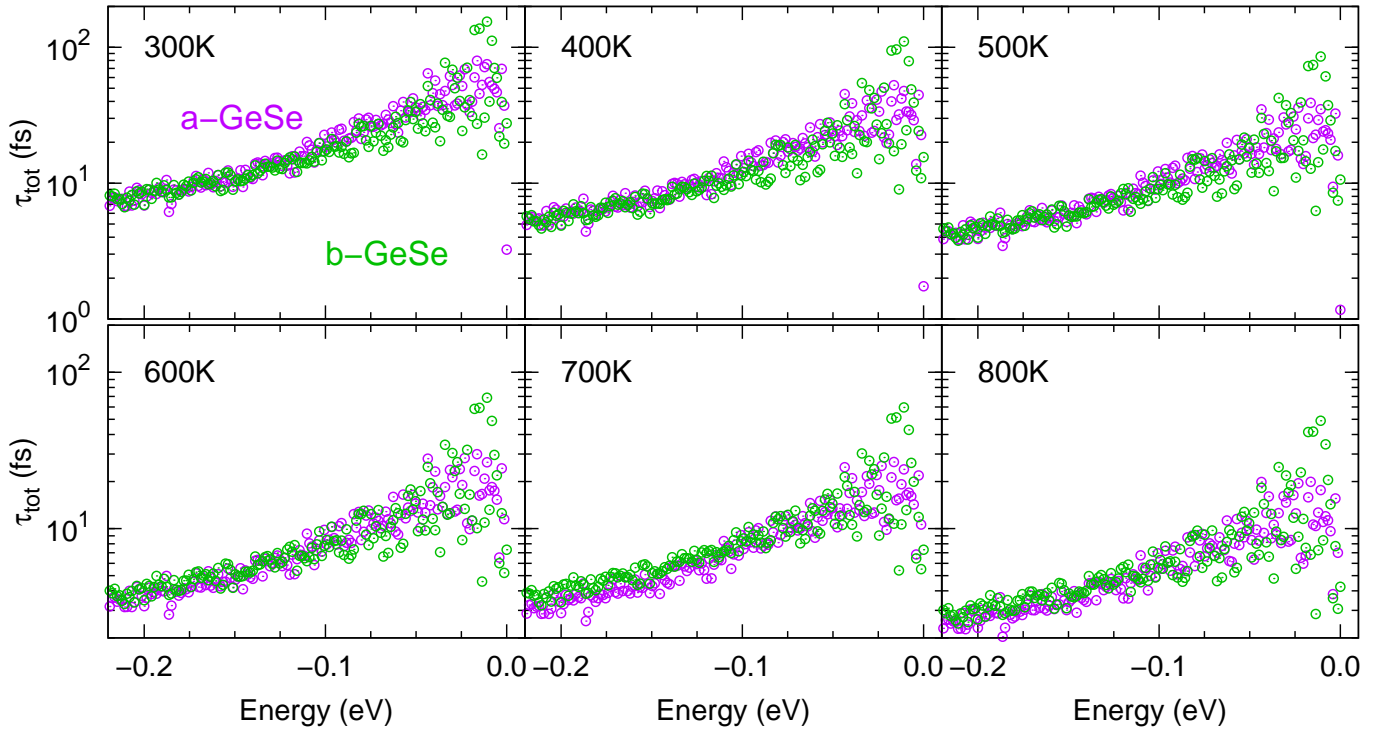


Fig. S5. Temperature dependence ( $T = 300\text{-}800$  K) of the total relaxation time ( $\tau_{\text{tot}}$ ) as a function of the hole energies for out-of-plane (a-axis) and in-plane (b-axis) p-doped GeSe.

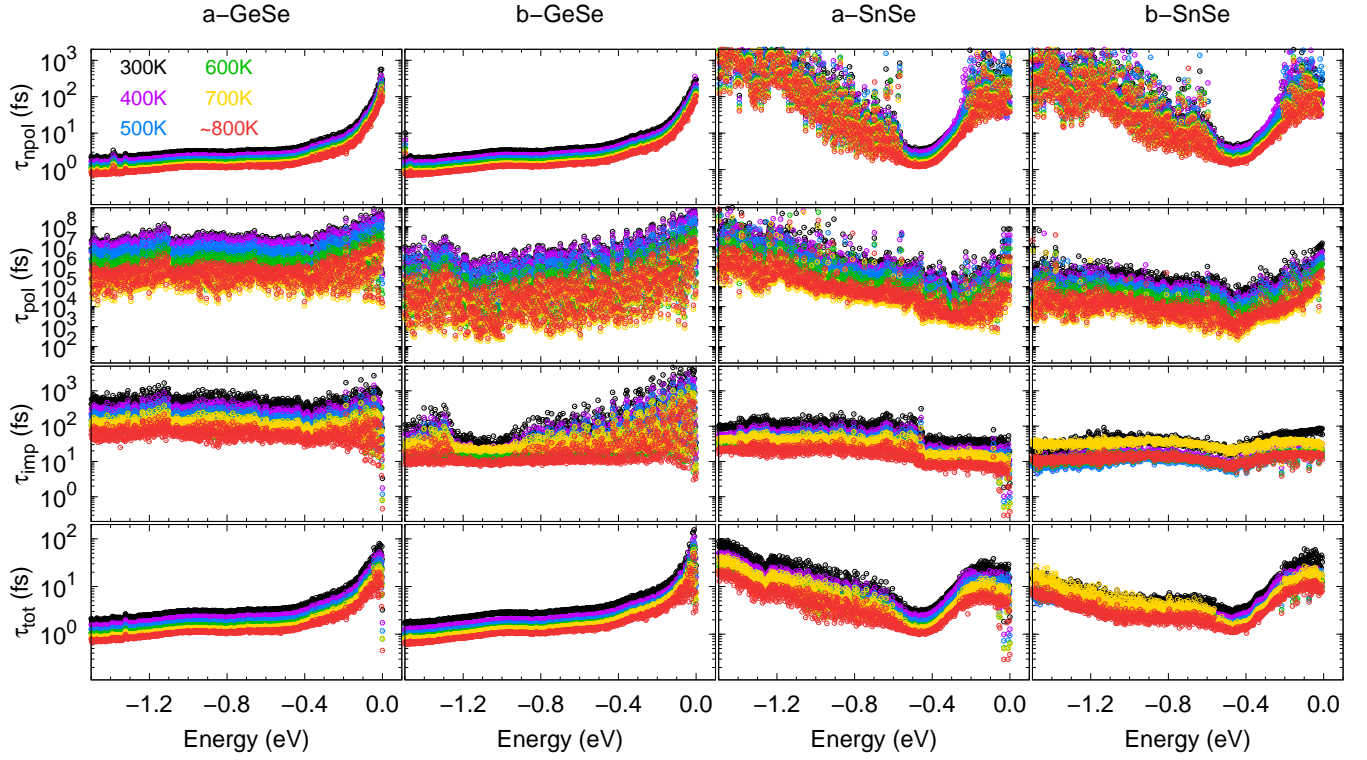


Fig. S6. Temperature dependence of the relaxation time as a function of hole energy for each of the scattering mechanisms: nonpolar scattering by phonons ( $\tau_{\text{npoh}}$ ), screened polar scattering by optical phonons ( $\tau_{\text{poh}}$ ), screened scattering by ionized impurities ( $\tau_{\text{imp}}$ ) and total scattering ( $\tau_{\text{tot}}$ ). Results are shown for p-doped GeSe (a- and b-axis) and p-doped SnSe (a- and b-axis). The hole density was derived from experimental transport data for the a-axis of p-doped SnSe as reported by Zhao *et al.*[19], as explained in the main text.

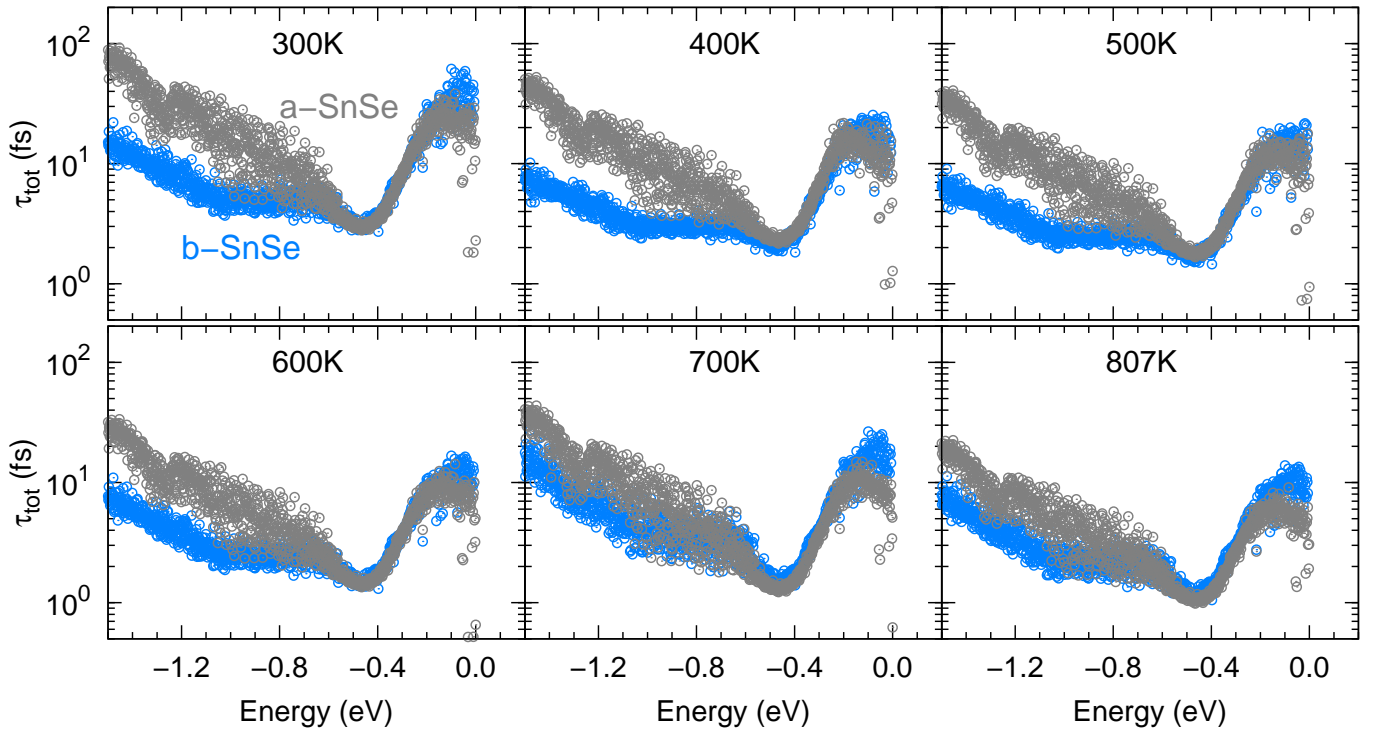


Fig. S7. Total relaxation time ( $\tau_{\text{tot}}$ ) as a function of hole energy for out-of-plane (a-axis) and in-plane (b-axis) p-doped SnSe at six temperatures between 300 and 807 K.

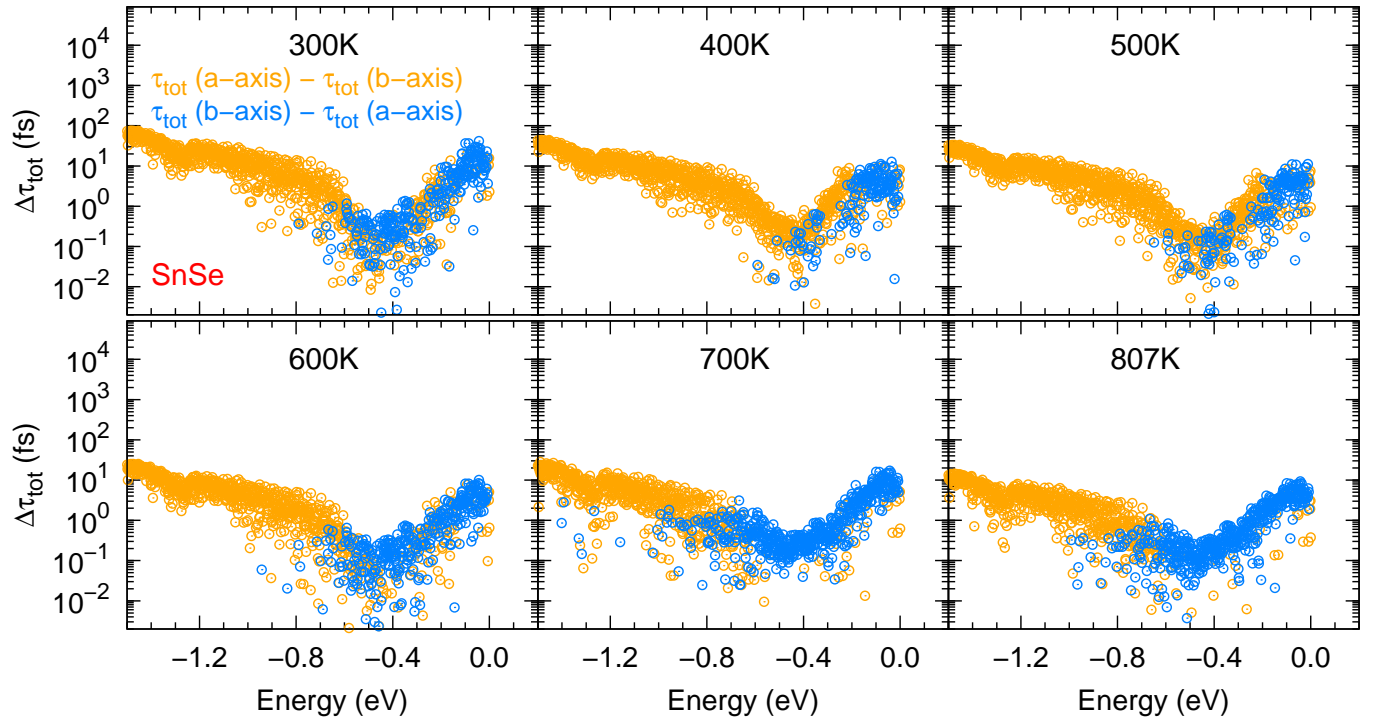


Fig. S8. Absolute value of the difference in total relaxation time,  $\Delta\tau_{\text{tot}}$ , between out-of-plane (a-axis) and in-plane (b-axis) p-doped SnSe as a function of hole energy for six different temperatures. Yellow (blue) points indicate that the a-axis RT is larger (smaller) than the b-axis RT.

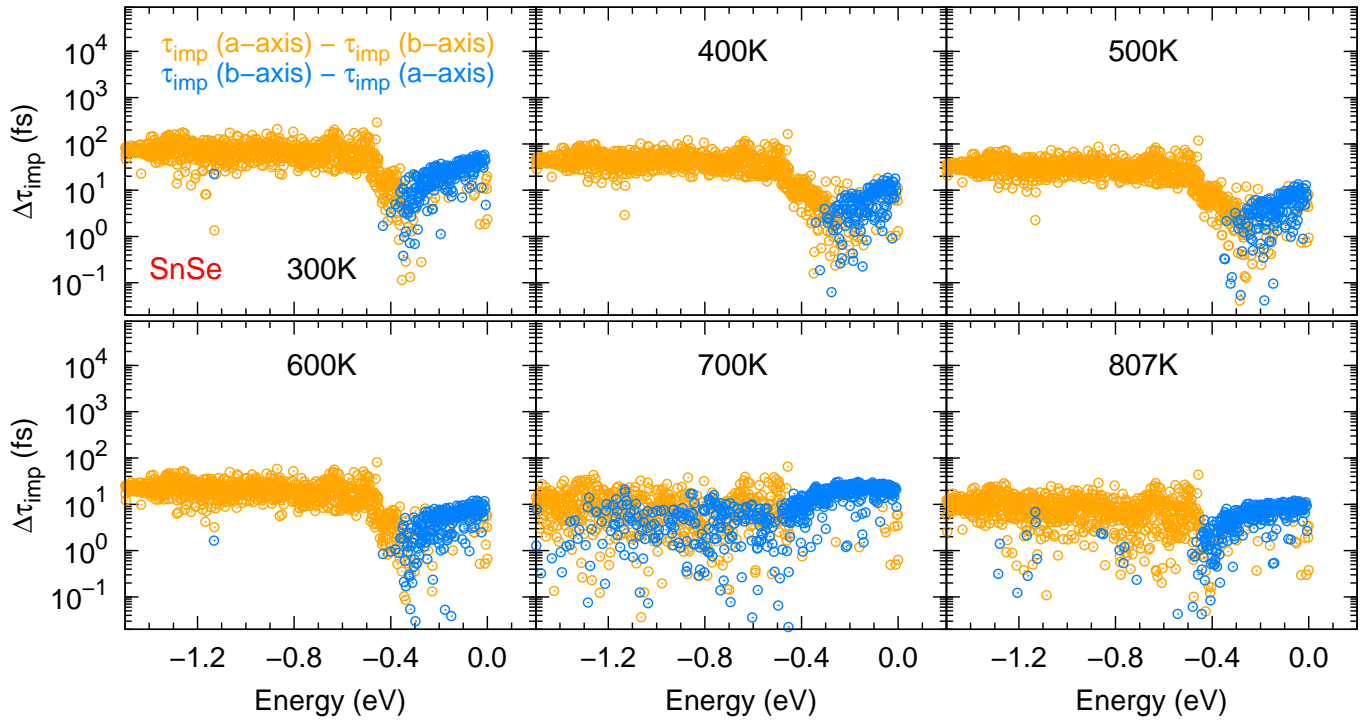


Fig. S9. Absolute value of the difference in relaxation time due to impurity scattering,  $\Delta\tau_{\text{imp}}$ , between out-of-plane (a-axis) and in-plane (b-axis) p-doped SnSe as a function of hole energy for six different temperatures. Yellow (blue) points indicate that the a-axis RT is larger (smaller) than the b-axis RT.

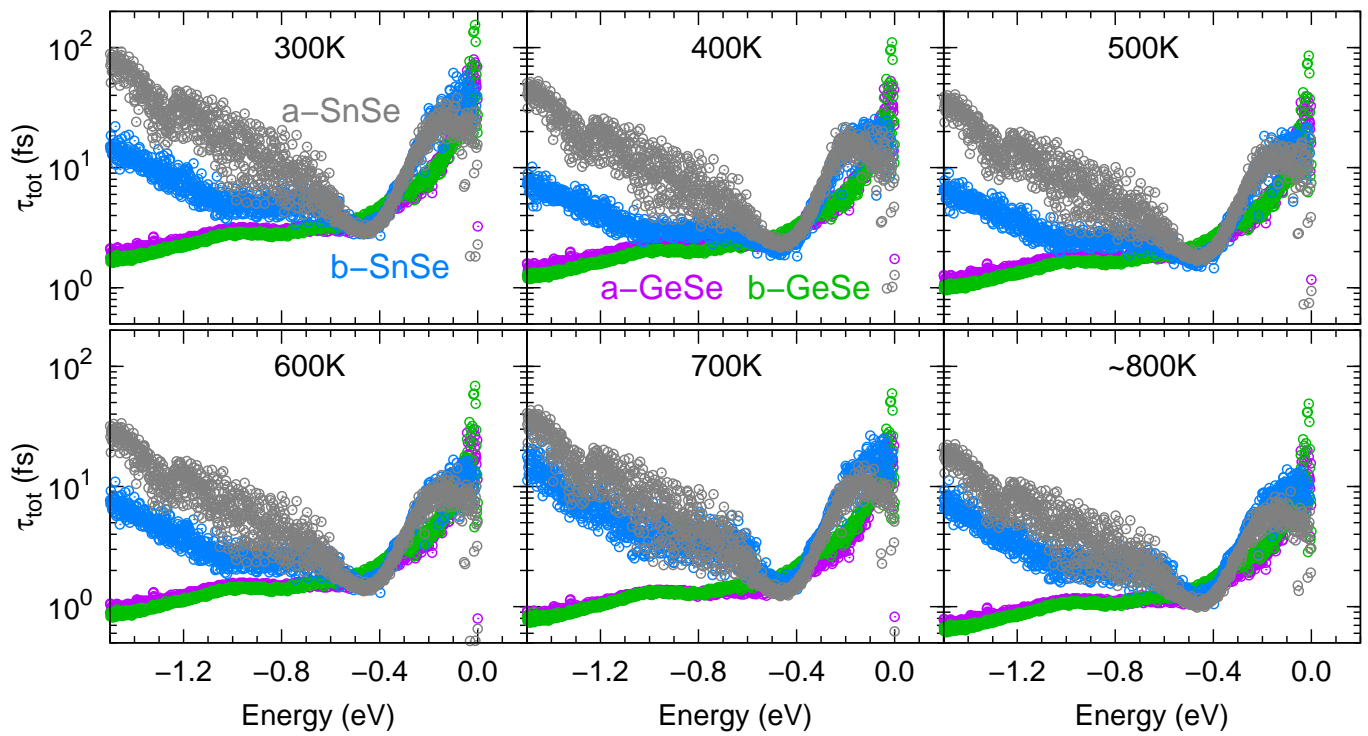


Fig. S10. Total relaxation time ( $\tau_{\text{tot}}$ ) as a function of hole energy for p-doped GeSe (a- and b-axis) and p-doped SnSe (a- and b-axis), for six different temperatures between 300 and 800 K. The hole density was derived from experimental transport data for the a-axis of p-doped SnSe as reported by Zhao *et al.*[19]

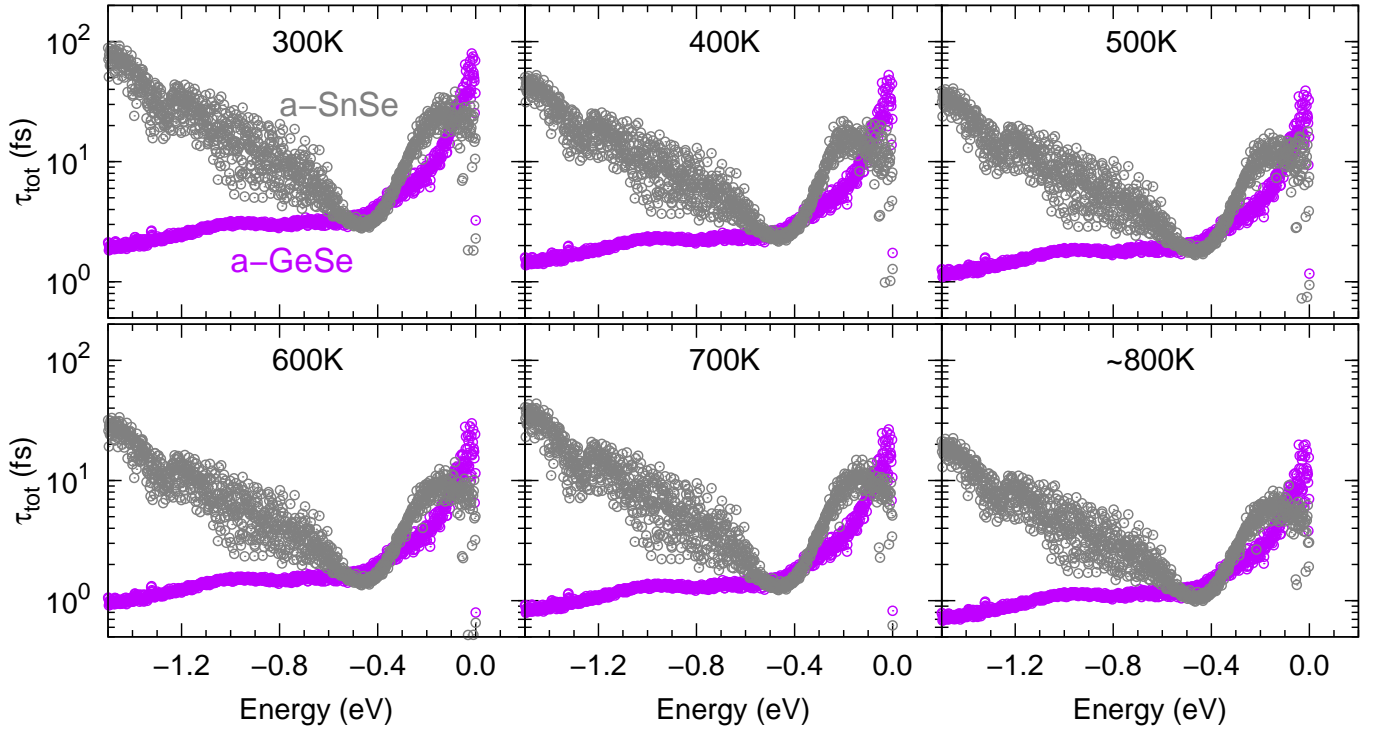


Fig. S11. Total relaxation time ( $\tau_{\text{tot}}$ ) as a function of hole energy for out-of-plane (a-axis) p-doped GeSe and SnSe for six different temperatures between 300 and 800 K.

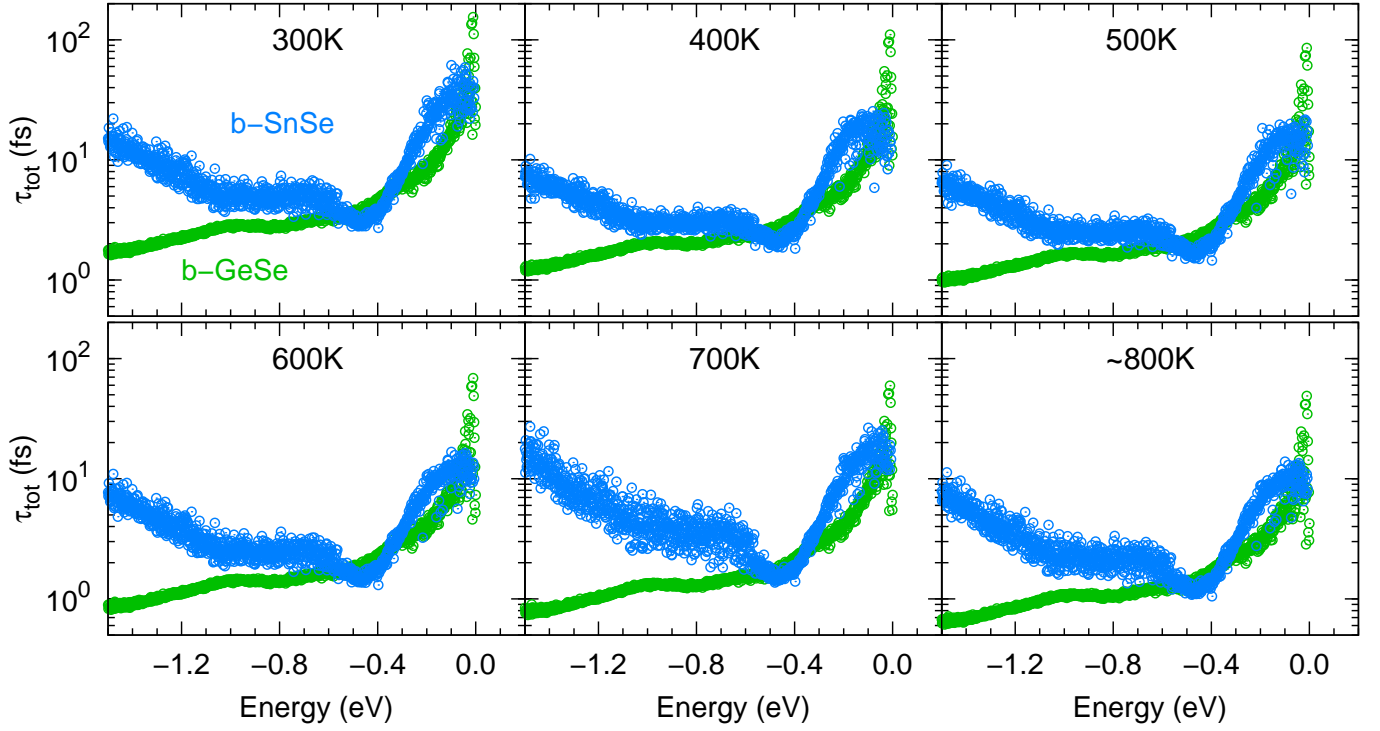


Fig. S12. Total relaxation time ( $\tau_{\text{tot}}$ ) as a function of hole energy for in-plane (b-axis) p-doped GeSe and SnSe for six different temperatures between 300 and 800 K.



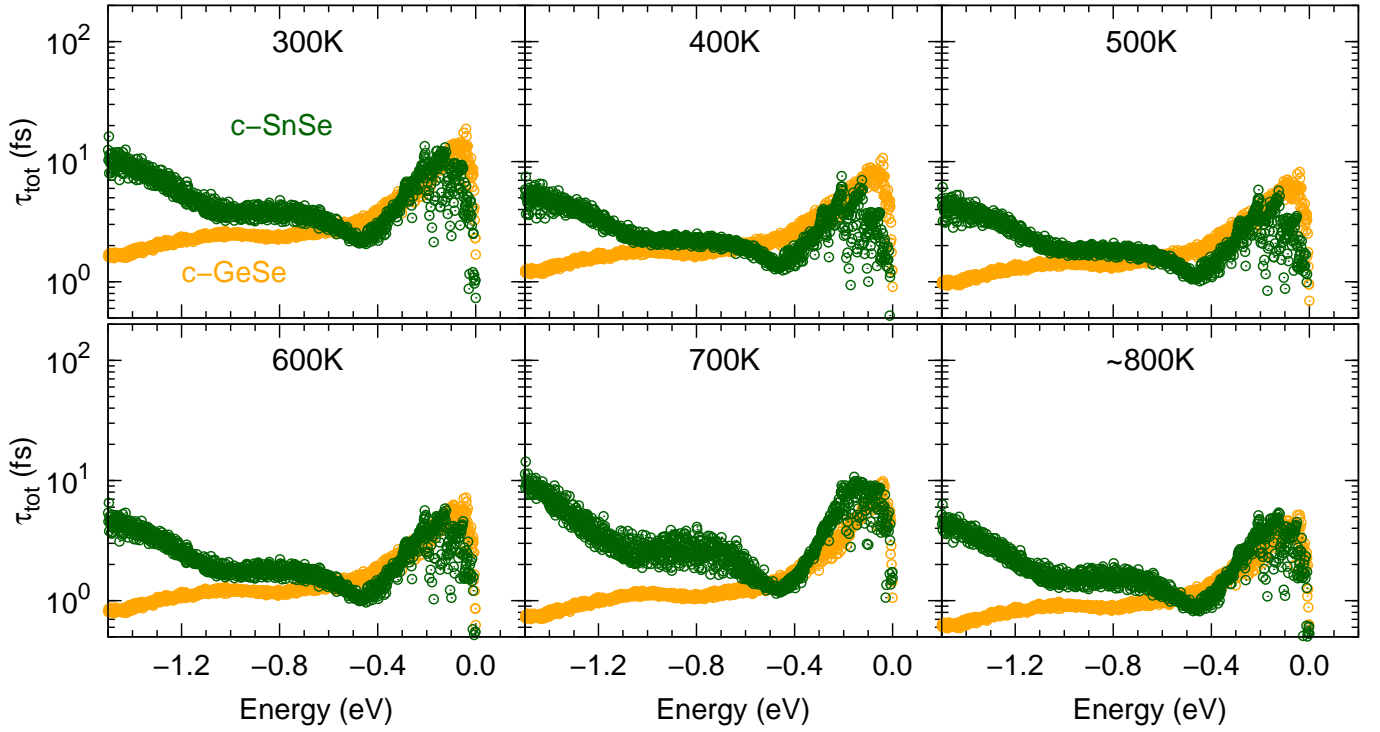


Fig. S13. Total relaxation time ( $\tau_{\text{tot}}$ ) as a function of hole energy for in-plane (c-axis) p-doped GeSe and SnSe for six different temperatures between 300 and 800 K.

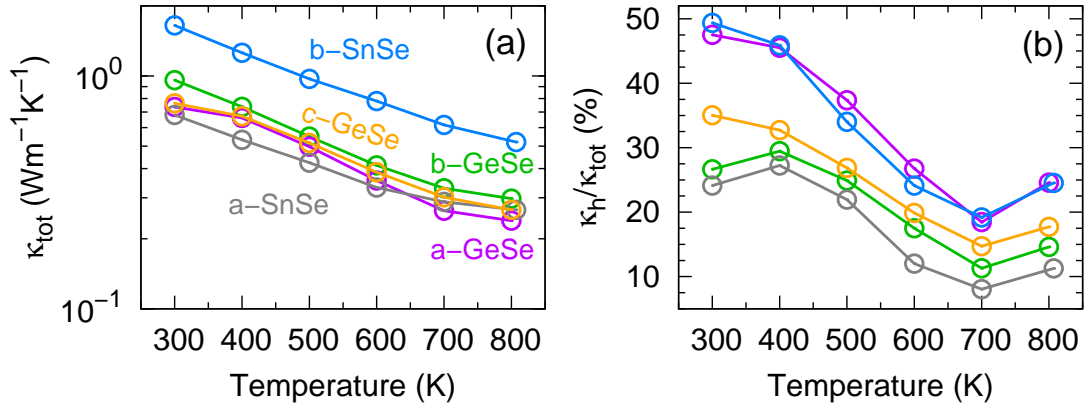


Fig. S14. (a) Total thermal conductivity,  $\kappa_{\text{tot}}$ , as a function of temperature for p-doped GeSe (all axes) and SnSe (a- and b-axis). The lattice thermal conductivities were derived from Hao et al.[20] (b) Fraction of the total thermal conductivity  $\kappa_{\text{tot}}$  contributed by holes, as a function of temperature.

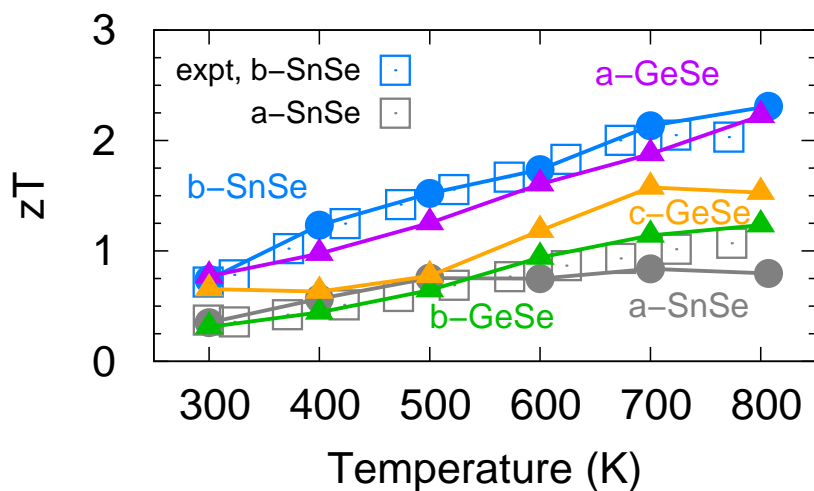


Fig. S15. Thermoelectric figure of merit ( $zT$ ) as a function of temperature for p-doped GeSe (all axes) and SnSe (a- and b-axis). The experimental data reported by Zhao *et al.*[19] for both axes of p-doped SnSe are shown for comparison. The GeSe transport properties were calculated using the temperature dependent carrier density and ionized impurity concentration derived from b-axis p-doped SnSe, also reported by Zhao *et al.*[19]

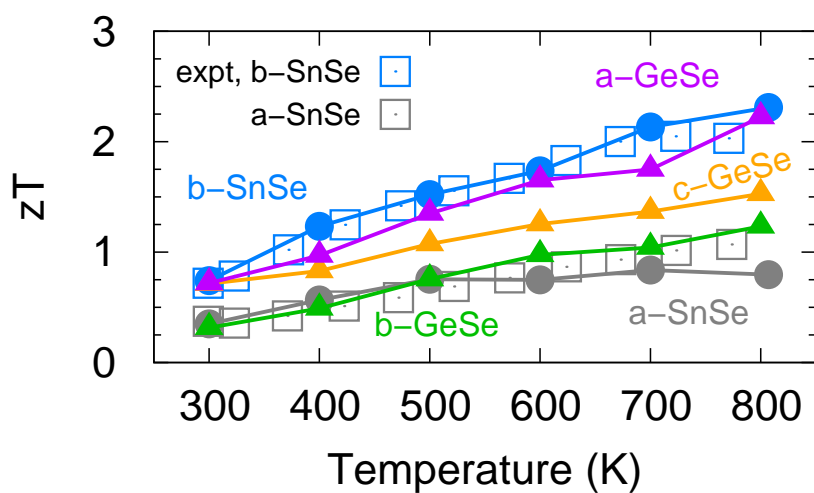


Fig. S16. Thermoelectric figure of merit ( $zT$ ) as a function of temperature for p-doped GeSe (all axes) and SnSe (a- and b-axis). The experimental data reported by Zhao *et al.*[19] for both axes of p-doped SnSe are shown for comparison. The GeSe transport properties were calculated using the temperature dependent carrier density and ionized impurity concentration derived from c-axis p-doped SnSe, also reported by Zhao *et al.*[19]

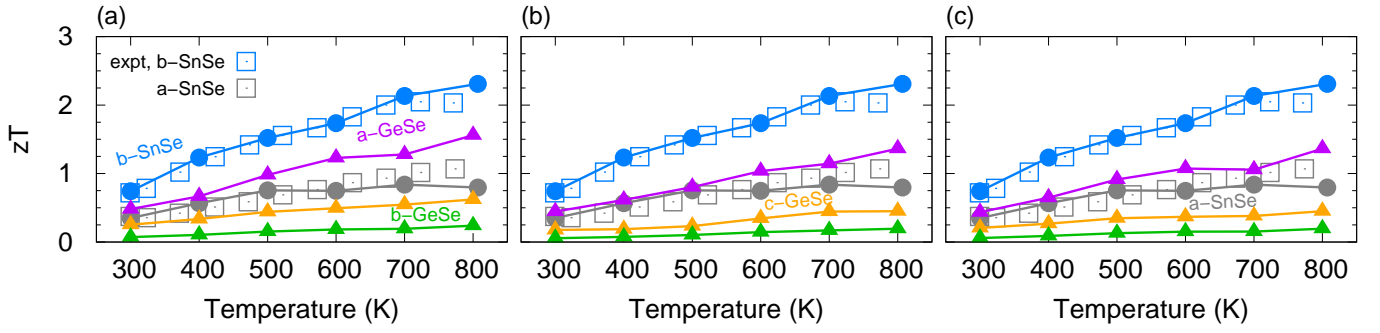


Fig. S17. Thermoelectric figure of merit ( $zT$ ) as a function of temperature for p-doped GeSe (all axes) and SnSe (a- and b-axis). The results for GeSe use values of  $\kappa_{\text{latt}}$  calculated by Yuan *et al.*[21]. The experimental data reported by Zhao *et al.*[19] for both axes of p-doped SnSe are shown for comparison. The GeSe transport properties were calculated using the temperature dependent carrier density and ionized impurity concentration derived from (a) a-axis (b) b-axis and (c) c-axis p-doped SnSe, also reported by Zhao *et al.*[19].

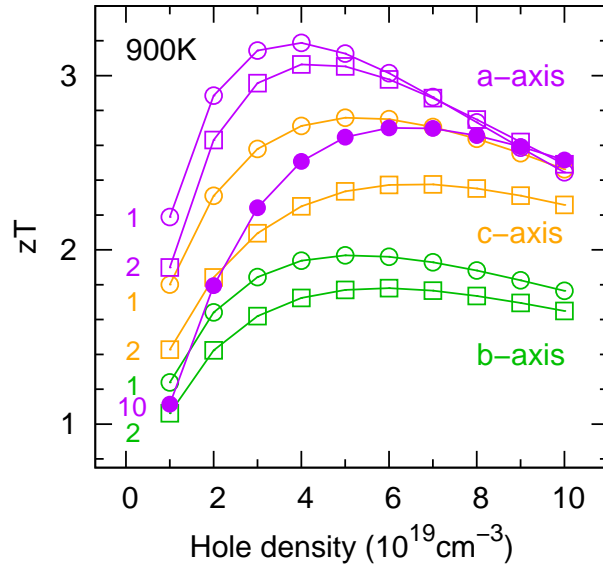


Fig. S18. Thermoelectric figure of merit,  $zT$ , as a function of hole density for fixed ratios  $n_{\text{ii}}/n_{\text{carr}} = 1, 2, 10$ , which label the left side of each curve corresponding to the a-, b- and c-axis of p-doped GeSe at 900 K.

- 
- [1] F. Giustino, *Reviews of Modern Physics* **89**, 015003 (2017).
- [2] S. Poncé, E. R. Margine, and F. Giustino, *Physical Review B* **97**, 121201 (2018).
- [3] S. Poncé, W. Li, S. Reichardt, and F. Giustino, *Reports on Progress in Physics* **83**, 036501 (2020).
- [4] H. Fröhlich, *Proc. Roy. Soc.(London)* **160**, 230 (1937).
- [5] C. Verdi and F. Giustino, *Physical Review Letters* **115**, 176401 (2015).
- [6] C. Pellegrini, A. Marinelli, and S. Reiche, *Reviews of Modern Physics* **88**, 015006 (2016).
- [7] C. Bostedt, S. Boutet, D. M. Fritz, Z. Huang, H. J. Lee, H. T. Lemke, A. Robert, W. F. Schlotter, J. J. Turner, and G. J. Williams, *Reviews of Modern Physics* **88**, 015007 (2016).
- [8] P. Vogl, *Physical Review B* **13**, 694 (1976).
- [9] N. Marzari and D. Vanderbilt, *Physical review B* **56**, 12847 (1997).
- [10] H. Ehrenreich, *Journal of Physics and Chemistry of Solids* **8**, 130 (1959).
- [11] A. S. Chaves, D. T. Larson, E. Kaxiras, and A. Antonelli, *Physical Review B* **104**, 115204 (2021).
- [12] H. Brooks, in *Advances in electronics and electron physics*, Vol. 7 (Elsevier, 1955) pp. 85–182.
- [13] D. Chattopadhyay and H. Queisser, *Reviews of Modern Physics* **53**, 745 (1981).
- [14] A. S. Chaves, R. L. González-Romero, J. J. Meléndez, and A. Antonelli, *Physical Chemistry Chemical Physics* **23**, 900 (2021).
- [15] B. M. Askerov and S. Figarova, *Thermodynamics, Gibbs Method and Statistical Physics of Electron Gases*, Vol. 57 (Springer Science & Business Media, 2009).
- [16] D. G. Shankland, in *Computational Methods in Band Theory* (Springer, 1971) pp. 362–367.
- [17] D. Koelling and J. Wood, *Journal of Computational Physics* **67**, 253 (1986).
- [18] A. S. Chaves, A. Antonelli, D. T. Larson, and E. Kaxiras, *Physical Review B* **102**, 125116 (2020).
- [19] L.-D. Zhao, G. Tan, S. Hao, J. He, Y. Pei, H. Chi, H. Wang, S. Gong, H. Xu, V. P. Dravid, C. Uher, G. J. Snyder, C. Wolverton, and M. G. Kanatzidis, *Science* **351**, 141 (2016).
- [20] S. Hao, F. Shi, V. P. Dravid, M. G. Kanatzidis, and C. Wolverton, *Chemistry of Materials* **28**, 3218 (2016).
- [21] K. Yuan, Z. Sun, X. Zhang, and D. Tang, *Scientific reports* **9**, 1 (2019).